

Evaluation of systematic shifts of the $^{88}\text{Sr}^+$ single-ion optical frequency standard at the 10^{-17} levelPierre Dubé,^{*} Alan A. Madej, Zichao Zhou, and John E. Bernard*Frequency and Time, Measurement Science and Standards Portfolio, National Research Council Canada, Ottawa K1A 0R6, Canada*

(Received 27 November 2012; published 7 February 2013)

An ion trap of the end-cap design was built recently at the National Research Council of Canada for improved control of the $^{88}\text{Sr}^+$ single-ion optical frequency standard systematic shifts. The uncertainty on the micromotion-induced shifts is smaller by more than four orders of magnitude when compared to our previous trap system and reaches a fractional frequency uncertainty of 1×10^{-18} . To obtain this low uncertainty level, the micromotion is minimized with trim electrodes and the trap is operated at a special frequency at which there is anticorrelation between the second-order Doppler and Stark shifts. This choice of operating frequency, determined by the differential scalar polarizability of the clock transition, yields a suppression by a factor of ≈ 28 in the combined micromotion shifts. Like many optical frequency standards, the dominant source of uncertainty in the new trap is the blackbody radiation shift. Its uncertainty has been reduced by an order of magnitude with a recent theoretical evaluation of the differential scalar polarizability of the clock transition. The fractional blackbody shift uncertainty, estimated using a model of the blackbody field at the ion, is 2.2×10^{-17} . The otherwise dominant electric quadrupole shift is reduced to below the 3×10^{-19} level with a cancellation method based on the average frequency of several pairs of Zeeman components. This method also cancels the tensor Stark shift and simplifies the description of the frequency shifts that are quantization-axis dependent. This paper provides a detailed description of the $^{88}\text{Sr}^+$ optical frequency standard uncertainty evaluation and the methods used to make the standard robust against changes in the trap environment. The total fractional frequency uncertainty of the $^{88}\text{Sr}^+$ ion for our current system is estimated at 2.3×10^{-17} . We also discuss the uncertainty evaluation of a recently reported measurement of the $^{88}\text{Sr}^+$ *S-D* clock transition made over a 2-month period by comparison with a maser referenced to the SI second. The frequency measured is 444 779 044 095 485.5(9) Hz, with an uncertainty limited by the evaluation of the maser frequency.

DOI: [10.1103/PhysRevA.87.023806](https://doi.org/10.1103/PhysRevA.87.023806)

PACS number(s): 42.62.Eh, 06.30.Ft, 42.62.Fi, 37.10.Ty

I. INTRODUCTION

The realization of increasingly more accurate and stable time and frequency standards has been very fruitful for the development of science and technology. Well-known benefits include the realization of SI units of time and length, navigation based on the Global Positioning System (GPS), network synchronization, geodesy, measurement of physical constants, and tests of fundamental physics theories [1]. Until a few years ago, the lowest uncertainty on the systematic shifts were realized by microwave cesium fountain clocks. The continued progress in understanding and controlling the systematic shifts in cesium fountains has brought the uncertainty evaluation of several devices below the 10^{-15} level and down to 2×10^{-16} in the best cases [2–6].

Optical frequency standards with resonance frequencies typically five orders of magnitude larger than the cesium microwave transition hold the promise for significant improvements in stability and accuracy. The actual improvements obtained, however, also depend on such factors as the number of atoms, the linewidth and stability of the probe laser source, the sensitivity of the atomic transition to external perturbations, and the control over those perturbations. Understandably, the difficulty in making absolute optical frequency measurements [7] and of comparing different optical frequencies has been a major obstacle for the progress of optical frequency standards and for their use as clocks.

This obstacle became a thing of the past in 2000 with the development of the femtosecond laser frequency comb (femtocomb) technology, which allows for a simple, direct, and reliable comparison of an optical frequency with either a microwave standard or another optical frequency standard [8–10]. Of special interest is the ability to make direct measurements of the absolute frequency of an optical standard with respect to microwave cesium clocks that define the SI second. The value of the femtocomb breakthrough was immediately appreciated by the optical frequency standards community and the uncertainty on the absolute frequency measurements of single-ion optical frequency standards decreased rapidly afterward [11–20].

Concurrently, the uncertainties on the systematic shifts of single-ion standards have become better understood and controlled. A few groups have now reported uncertainties lower than the best cesium clocks [21–24], down to the upper 10^{-18} level for the Al^+ ion [25,26]. The expectation that the uncertainty of single-ion optical frequency standards could reach the 10^{-18} level is becoming a reality [27].

The idea of neutral atoms confined in optical lattices to realize an optical clock emerged shortly after the development of the femtocomb laser technology [28]. These so-called optical lattice clocks aim to combine the benefits of trapping and confinement found in single-ion standards and the large number of atoms found in cesium clocks. Their progress has also been impressive during the last decade [29], with systematic shift evaluations at the 10^{-16} level reported in the last few years [30–34]. Although the uncertainty evaluation of optical lattice clocks is currently an order of magnitude

^{*}pierre.dube@nrc-cnrc.gc.ca

larger than that of the best single-ion standards, they can provide better stability [29,35]. Reduction of the systematic shifts in lattice clocks is ongoing and could reach levels comparable to those of the single-ion standards in the future [29,36,37].

The high accuracy and stability of the optical frequency standards relies heavily on the performance of the laser systems used for probing the Hz-level resonances. The low data collection rates observed with single-ion standards and the high stability offered by the neutral atom clocks both demand probe laser systems with Hz-level linewidths, or lower, and high stability for optimum performance. The ongoing quest for narrower and more stable laser systems continues to be crucial for the development and performance of the optical frequency standards [38–46].

One atomic system of interest for the realization of an optical frequency standard is the $5s\ ^2S_{1/2} - 4d\ ^2D_{5/2}$ electric-quadrupole transition of a trapped and laser-cooled single ion of $^{88}\text{Sr}^+$. This single-ion reference has been studied for a number of years by our group at the National Research Council of Canada (NRC) [13,47,48] and by the group at the National Physical Laboratory (NPL) in the United Kingdom [12]. During the last few years, a few other groups have also made contributions studying the $^{88}\text{Sr}^+$ ion [49–52].

We have recently completed the construction of a new trap system aimed at reducing the dominant systematic shifts observed in our previous ion trap. In contrast with the previous system, where only a single optical access port was available [13,53], the new system uses an ion trap of the end-cap design [54] and provides access ports for laser beams along three mutually orthogonal directions. This important improvement makes it possible to minimize and evaluate the micromotion shifts and measure the ion temperature accurately. Another significant improvement for reduction of the micromotion shifts is the use of a trap frequency where the second-order Doppler shift and the scalar Stark shift cancel each other by a factor of 28 (see Sec. IV B5), as determined by the current uncertainty in the differential scalar polarizability of the S - D clock transition [55]. The combined use of micromotion minimization and the special choice of trap frequency yields an uncertainty of 1×10^{-18} in the micromotion shifts, a reduction by more than four orders of magnitude compared to the previous trap [13].

At present, the most important contribution to the $^{88}\text{Sr}^+$ ion frequency uncertainty is the blackbody radiation shift. To evaluate this shift with low uncertainty it is necessary to have accurate scalar polarizability coefficients for the clock transition and to evaluate the blackbody radiation field at the ion. An order of magnitude reduction in the uncertainty of the polarizability coefficients was obtained with a recent theoretical evaluation [55]. In addition, the end-cap trap was designed with highly polished and reflective molybdenum end-cap electrodes that lower the emissivity and reduce the effect of electrode heating on the blackbody field. The open and simple geometry of the trap combined with the high reflectivity of the electrodes has permitted the evaluation of the blackbody shift to an accuracy limited by the current knowledge of the differential scalar polarizability coefficients. The total blackbody radiation shift evaluation has a fractional frequency uncertainty of 2.2×10^{-17} .

Besides the main improvements highlighted above, a detailed presentation of the evaluation of the systematic shifts of the NRC $^{88}\text{Sr}^+$ ion is given in this paper. It is found that the total ion-related uncertainty is 2.3×10^{-17} , an order of magnitude lower than previously reported for the $^{88}\text{Sr}^+$ ion [12]. This uncertainty evaluation is also an order of magnitude lower than achieved by state-of-the-art cesium fountain clocks and it compares favorably with the leading ion frequency standards [25,26,56].

The uncertainty level reported here is by no means a fundamental limit for the $^{88}\text{Sr}^+$ ion system, as the scalar polarizability coefficients required for the evaluation of the blackbody shift can, in principle, be improved with suitable experiments and further theoretical evaluations based on new atomic data. An uncertainty evaluation for the $^{88}\text{Sr}^+$ ion system below the 10^{-17} level is expected to be within reach in the near future.

A measurement of the absolute frequency of the $^{88}\text{Sr}^+$ S - D clock transition was reported recently [48]. The measurements were made during a 2-month period by comparing to a maser referenced to the SI second by frequency transfer using Precise Point Positioning. The frequency obtained is 444 779 044 095 485.5(9) Hz, limited by the evaluation of the maser frequency at 2 parts in 10^{15} using circular-T reports from the Bureau International des Poids et Mesures (BIPM). Details of this measurement and associated uncertainty budget are also discussed in this work.

II. $^{88}\text{Sr}^+$ ION FREQUENCY STANDARD

Figure 1 is a partial energy level diagram of the $^{88}\text{Sr}^+$ ion showing the laser wavelengths used to operate the standard.

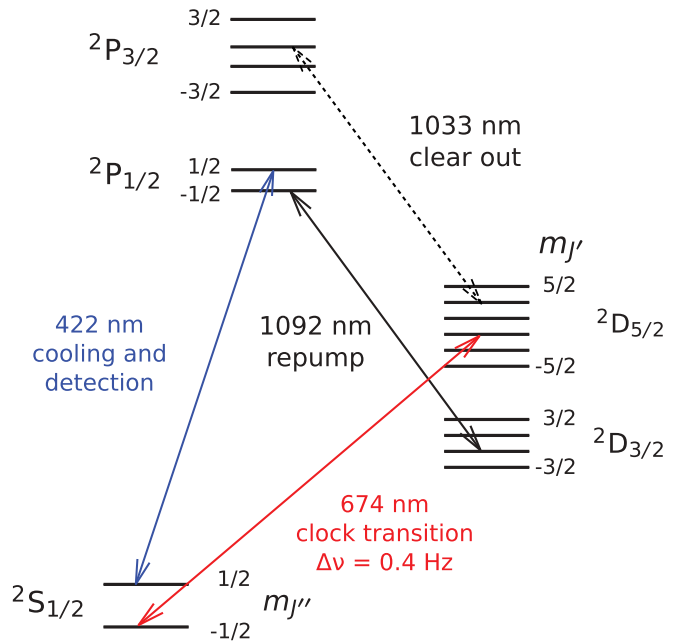


FIG. 1. (Color online) Partial energy level diagram of the $^{88}\text{Sr}^+$ ion. The solid arrowed lines show the transitions required for the operation the frequency standard. The dashed line indicates a transition that can be used to depopulate quickly or “clear out” the metastable $^2D_{5/2}$ state after a shelving event.

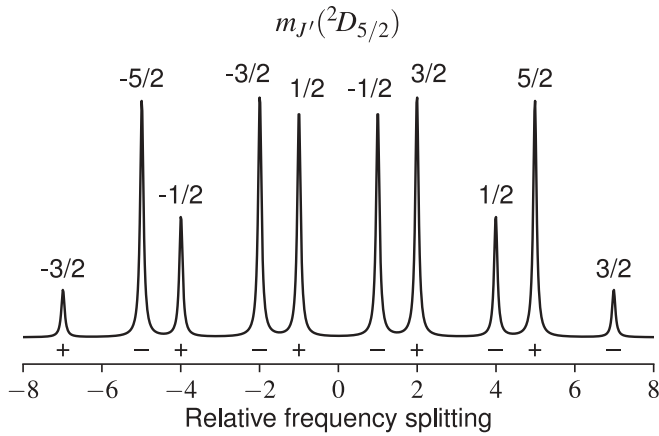


FIG. 2. Calculated Zeeman spectrum of the S - D clock transition. The magnetic quantum numbers in the ${}^2D_{5/2}$ state are displayed above the Zeeman components. Notice that each symmetric pair has the same $|m_{J'}|$. The magnetic quantum numbers in the ${}^2S_{1/2}$ state are shown below the components; the + and - signs indicate whether $m_{J''} = +1/2$ or $-1/2$.

The reference or clock transition is the electric-quadrupole allowed $5s\ {}^2S_{1/2} - 4d\ {}^2D_{5/2}$ transition at 674 nm. It has a natural linewidth of 0.407(2) Hz [57,58] and a quality factor of $Q = 1 \times 10^{15}$.

When subjected to a magnetic field, the S - D transition splits into ten Zeeman components shifted symmetrically about the zero-field line center as shown in Fig. 2. There is no magnetic insensitive component, but the linear Zeeman shift can be removed by measuring the average frequency of a symmetric pair of components [47]. For the measurements reported in this paper, the frequencies of three pairs of components were averaged to also cancel the electric quadrupole shift [13,59].

The ion kinetic motion is cooled using a 422-nm laser red-detuned from the strongly allowed $5s\ {}^2S_{1/2} - 5p\ {}^2P_{1/2}$ dipole transition. Since the upper state of the cooling transition can decay to the metastable $4d\ {}^2D_{3/2}$ state, it is necessary to use a repumper laser at 1092 nm to keep the ion into the S - P cooling branch.

The ion state following each probe pulse is detected using the electron shelving or quantum jump method [27]. The photons scattered by the ion at 422 nm during a cooling pulse indicate whether the ion is in the ground state (strong fluorescence) or has been excited to the metastable ${}^2D_{5/2}$ state, in which case a low level of photons scattered by the trap electrodes is detected. Each transition from the ground state to the metastable state is counted as a single quantum jump event.

The quantum jump rate is determined by the interaction strength between the probe laser source and the clock transition and varies according to the resonance line shape. For example, the spectrum of a component of the clock transition can be obtained by recording the quantum jump rate as a function of detuning, as shown in Fig. 3.

To stabilize the laser to a Zeeman component, the quantum jump rate is measured at two frequencies typically separated by the resonance linewidth. From the difference in the rates observed on each side of the transition, a frequency error signal is obtained and applied to the laser to realize the

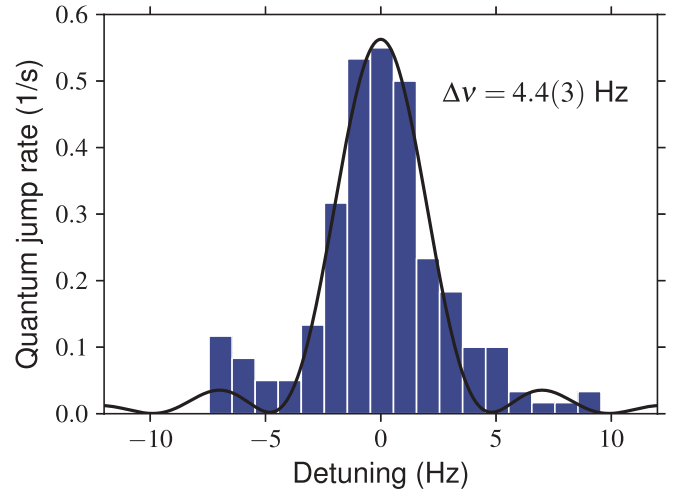


FIG. 3. (Color online) High-resolution spectrum of a Zeeman component of the ${}^{88}\text{Sr}^+$ ion S - D clock transition recorded at low laser intensity. The histogram shows the quantum jump rate as a function of frequency detuning while the solid curve is a Rabi excitation spectrum computed by solving the optical Bloch equations for a 200-ms probe pulse.

lock [47]. As mentioned earlier, three pairs of components are usually measured during the lock runs to eliminate the linear Zeeman shift and the electric quadrupole shift. Each of the six components is measured independently and the resulting line centers are combined by averaging to yield the clock transition line center.

An optional laser at 1033 nm can be used to return quickly the ion to the ground state once the ion state has been determined by the fluorescence signal. Such a laser improves the quantum jump rate and therefore the stability of the lock to line center. This laser was not used in the present experiments.

III. EXPERIMENTAL APPARATUS

A. End-cap trap

In the new trapping apparatus, the single ion of ${}^{88}\text{Sr}^+$ is confined in a miniature radio-frequency trap of the end-cap design [54]. A schematic diagram is shown in Fig. 4. It is built with end-cap electrodes made with 0.50-mm-diameter molybdenum wires. Their end faces, polished to a mirror finish, are separated by 0.54 mm. The shield electrodes located over the end-cap wires were made from tantalum tubes of 2.00 mm outside diameter and 1.00 mm inside diameter. Alumina tubes were inserted between the shield and end-cap electrodes for electrical insulation and mechanical centering. The end-cap trap structure is built entirely with nonmagnetic materials.

The trap is operated by applying a voltage of 212(4) V amplitude at a frequency of 14.39 MHz between the shield and end-cap electrodes. For these operating conditions, the axial secular frequency is $\omega_Z \approx 2\pi \times 2.3$ MHz and the radial secular frequencies are $\omega_X, \omega_Y \approx 2\pi \times 1.2$ MHz. ω_X and ω_Y actually differ by about $2\pi \times 20$ kHz due to trap asymmetries.

The ion position in the trap axial direction is controlled by applying a small dc voltage between the end cap electrodes. In the radial direction, the ion position is controlled with two mutually orthogonal trim electrodes located 5 mm from the

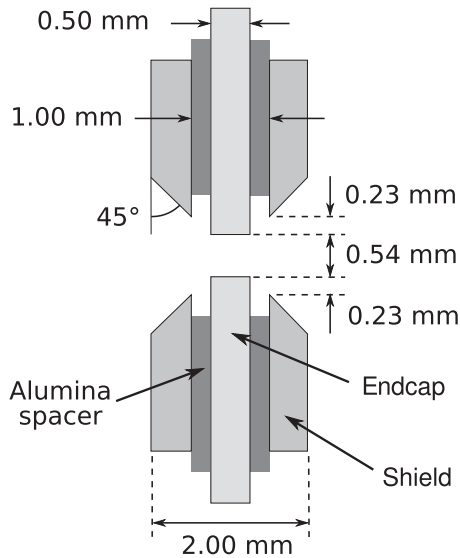


FIG. 4. Cross-section of the NRC end-cap trap electrodes. The lengths along the trap axis are not shown to scale.

trap center. They are made from 2.00-mm-diameter tantalum rods that are also used to improve the rigidity of the trap structure.

$^{88}\text{Sr}^+$ ions are loaded into the trap by photoionizing neutral strontium atoms emitted by a small oven that contains a mixture of SrAl_4 and Ni powder [57]. The ionization is achieved by a two-step, doubly resonant process in which the atoms are excited to an autoionizing state [60,61]. The first excitation step, on resonance with the $5s^2\ ^1S_0-5s5p\ ^1P_1$ transition of strontium at 461 nm, is performed with a frequency-doubled extended-cavity diode laser system [62]. The second step, from the intermediate $5s5p\ ^1P_1$ state to the autoionizing $(4d^2 + 5p^2)\ ^1D_2$ state, is driven by a free-running 405-nm diode laser. The photoionizing laser beams are turned off as soon as the trap is loaded with a single ion.

In a test setup, we have determined the relation between the oven temperature and the heating current passing through a tantalum wire spot-welded to the oven. Combining these data with the temperature dependence of the strontium vapor pressure [63], we found that photoionization loading is at least three orders of magnitude more efficient than electron bombardment loading, the method used in the previous NRC trap system [13,53]. The absence of an electron beam aimed at the trap and the reduction of deposited strontium metal on the electrodes with photoionization loading contribute to reduce the formation of patch potentials and charge buildup on the trap structure. The benefits are an improved stability of the micromotion compensation and of the electric quadrupole shift magnitude, and a reduction in the ion heating rate [1,61,64].

The trap is housed in a vacuum chamber made with nonmagnetic stainless-steel that provides a total of 10 ports for fluorescence collection, electrical feedthroughs, a vacuum pump, and laser access along three orthogonal directions. The background gas pressure in the ultrahigh-vacuum chamber is ≈ 16 nPa, mostly from H_2 gas.

The ac and dc magnetic fields from the laboratory environment are suppressed with two concentric mu-metal magnetic shields. A residual field of $2.025(3)\ \mu\text{T}$ remains, caused by

magnetic parts on the vacuum chamber. This background field was used for splitting the Zeeman components of the clock transition in the frequency measurements reported here. Variations in the background magnetic field, monitored by the splitting of the Zeeman components, are on the order of 100 pT per hour. For the most magnetic-sensitive Zeeman components used in the present experiments, 100 pT/h translates into a splitting drift rate of 1.5 mHz/s.

For complete control over the magnetic field at the ion, three pairs of Helmholtz coils are mounted on the laser-beam access ports. They were used to determine the direction of the background field and to vary the quantization axis direction during the evaluation of the magnitude of the electric field gradient at the ion.

The quantum jumps are monitored by recording the ion fluorescence signal with a photomultiplier tube (PMT). The 422-nm fluorescence is collected with a high numerical aperture lens ($\text{NA} \approx 0.5$) mounted inside the vacuum chamber for high collection efficiency. Outside the vacuum chamber, the collimated light passes through a series of baffles and a narrow-bandpass filter (Iridian Spectral Technologies) to prevent scattered light from the other laser sources from reaching the PMT. Only light at 405 nm causes a slight increase in the background signal during loading. The filter is characterized by a peak transmission of 95% and a bandwidth of 0.23 nm full width at half maximum (FWHM), centered at the fluorescence wavelength of 421.7 nm by angle tuning. With this filter, the ion fluorescence can be monitored during the loading process. The filtered light is focused with a camera lens onto a $150\text{-}\mu\text{m}$ pinhole placed in front of the PMT. The pinhole position is centered on the ion image with micrometer screws to maximize the fluorescence-to-background ratio. In our experiments, the detection rate is typically 6000 to 8000 photons per second and the background is on the order of 100 photons per second.

A high-sensitivity CCD camera is mounted opposite the PMT port to observe the ion motion and displacement. A 100-mm, $f/4$ camera lens mounted outside the port window collects the ion fluorescence and forms an image 50 cm from the ion where a $3\times$ microscope objective magnifies the secondary image onto the camera sensor. The total magnification is $13.6\times$ and each of the $16 \times 16\ \mu\text{m}^2$ pixel images an area of $1.2 \times 1.2\ \mu\text{m}^2$ at the plane of the ion. The resolution limit of the camera lens is $\approx 3\ \mu\text{m}$ or three pixel widths in the current setup. A narrow bandpass filter identical to the one described above for the PMT setup is inserted before the secondary image. The infrared sensitivity of the CCD sensor required an additional filter to cut off the 1092-nm scattered light. The camera is routinely used for coarse minimization of micromotion as described in Sec. IV B 2.

B. Laser systems

A measurement cycle requires nonoverlapping cooling and probing laser pulses to prevent large ac-Stark shifts of the clock transition. In the frequency measurements reported in this paper, the cooling pulse, which includes the 422- and 1092-nm radiations, is 30 ms long, while the probe pulse is 100 ms long. To ensure that the ion has returned to the ground state before the 674-nm probe pulse begins, the 1092-nm

TABLE I. Laser-beam parameters. λ is the laser wavelength and w_0 the beam radius at the ion. The *Cooling period* and *Probing period* columns designate the part of the measurement cycle when the power and intensity are evaluated.

λ (nm)	w_0 (μm)	Cooling period		Probing period	
		(μW)	(kW/m^2)	(nW)	(W/m^2)
422	16(1)	0.4(1)	1.0(3)		$7(7) \times 10^{-10}\text{a}$
674	32(5)			0.03(1)	0.02(1)
1092	51(2)	4(1)	1.0(3)	6(2)	1.5(5)

^aEstimate of the 422-nm scattered light intensity.

pulse is made slightly longer than the 422-nm pulse. Buffer times of $\simeq 3$ ms are used between the cooling and probing pulses to again prevent ac-Stark shifts that could result from incompletely attenuated beams during the turn-off transition. Table I provides a summary of the beams radii, powers, and intensities during cooling and probing for evaluation of the Stark shifts in Sec. IV D. The intensities and detunings of the 422- and 1092-nm cooling lasers were chosen to optimize ion fluorescence and cooling efficiency [52]. The applied Rabi frequencies on the cooling and repumper transitions were, respectively, 1.6Γ and 2Γ , where $\Gamma = 135.58 \times 10^6/\text{s}$ is the decay rate of the $^2P_{1/2}$ state [55].

The spectrally ultranarrow 674-nm probe light is realized with an extended-cavity diode laser locked to a reference Fabry-Perot cavity fabricated with ultralow expansion (ULE) glass material. The spectral characteristics and drift rate of the laser are determined by the noise and creep of the reference cavity. For maximum stability, the 25-cm cavity is enclosed in a vacuum vessel stabilized at the temperature where the thermal expansion coefficient of the ULE is zero. There is essentially no drift caused by temperature variations in our setup, but there remains a small isothermal creep that causes a drift rate of ≈ 10 mHz/s. The laser linewidth obtained with this reference cavity is 4.4(3) Hz as shown in Fig. 3. A phase-noise cancellation system was implemented to obtain this narrow linewidth on the laser beam delivered to the ion trap setup by optical fiber [65,66].

The probe laser is locked to the longitudinal cavity mode that is the closest to the S - D transition frequency. The difference is covered by shifting the laser frequency with a double-pass acousto-optic modulator (AOM) driven by a signal generator referenced to a maser signal. This setup, controlled by a computer, allows precision tuning of the laser frequency for spectroscopic measurements and for locking to the transition line center. The double-pass AOM also serves as a chopper for the probe laser beam.

Note that in a frequency measurement, it is the unshifted probe laser frequency determined by the ULE cavity that is measured with a femtocomb referenced to a maser. The lock to the ion line center, realized by tuning the AOM, measures the frequency difference between the ULE and the ion. The ion frequency is then obtained by combining the femtocomb and AOM frequency data. For further information about the probe laser system, the reader is referred to previous work [42].

The 422-nm extended-cavity diode laser is offset locked using a double-pass AOM to a saturated absorption resonance

of ^{85}Rb [67,68]. Optimum cooling is obtained by adjusting the detuning from the S - P transition with the AOM frequency. The laser routinely stays locked to ^{85}Rb for more than a day before a mode-hop occurs. We have demonstrated continuous trapping of a single ion for a period of up to 8 days with this system.

Resonant radiation at 422 nm during the probe pulse would have a serious impact on the uncertainty of the clock transition frequency because of the large ac Stark shifts that would appear on the $^2S_{1/2}$ state. For this reason, the 422-nm power, which is delivered to the ion trap by optical fiber, is chopped using a galvomotor actuated aluminum blade before the fiber coupling stage. This provides complete extinction of the 422-nm light on the fiber output.

It is also possible that light at 422 nm, scattered by the chopper blade or by other components of the cooling laser apparatus, reaches the ion via the optical access ports on the vacuum chamber. In our setup, the scattered light intensity at the ion is expected to be extremely small for the following reasons: Multiple reflections are required, the cooling laser system is mounted on a separate optical table located a few meters away from the ion trap, and the solid angle subtended by each of the ion trap optical ports is restricted to 0.006 sr by the magnetic shields openings. We have made measurements to estimate the scattered 422-nm laser intensity at the ion using a 1 cm^2 photodetector subtending a solid angle of 3 sr to increase the detection sensitivity. No light at 422 nm was detected near the vacuum chamber ports. An upper limit of the intensity is given by the $50\text{ nW}/\text{m}^2$ resolution of the measurements. After taking into account the solid angle differences between the photodetector and the total optical access on the ion trap apparatus, we estimate that the 422-nm light intensity at the ion is less than $0.7\text{ nW}/\text{m}^2$.

The 1092-nm repump radiation is obtained from a diode-pumped, ytterbium-doped fiber laser. Its single-mode frequency is stabilized and tuned relative to a reference polarization-stabilized helium-neon laser using a transfer Fabry-Perot cavity [69]. This locking scheme ensures long-term operation and wide tunability of the laser frequency. An AOM is used for chopping the 1092-nm radiation during the measurement cycle. The attenuation of the first-order diffracted beam is 28 dB when the rf power to the AOM is turned off. The imperfect attenuation accounts for the nonzero 1092-nm power level reported in Table I in the *Probing period* column.

The 674- and 422-nm laser beams are spatially overlapped, then split and aligned for intersection with the ion along three mutually orthogonal directions. The 674-nm beams are used for measurement of the ion temperature and micromotion by the method of sideband spectroscopy. The 422-nm beams are expected to provide more efficient cooling of the ion than would a single beam by not relying on coupling between the different modes of the secular motion. The 1092-nm beam is overlapped with the other beams along only one direction.

IV. FREQUENCY SHIFTS

In this section we discuss the known shifts of the $^{88}\text{Sr}^+$ ion S - D electric-quadrupole transition. To make a clear statement about the $^{88}\text{Sr}^+$ ion performance as a frequency standard, only

the shifts directly related to the ion and its environment are considered here. The systematic shifts and uncertainties caused by measurement issues are discussed separately, in the context of the absolute frequency measurement of Sec. V.

A. Electric quadrupole shift

The electric quadrupole shift is the largest frequency shift in our end-cap trap if any of the symmetric Zeeman pairs is taken separately. To first order in perturbation theory, the frequency shift Δf_Q of a magnetic sublevel $m_{J'}$ caused by the interaction between the quadrupole moment and an electric field gradient is given by [13,70,71]

$$\Delta f_Q = \frac{1}{4} \nu_Q (3 \cos^2 \theta - 1) \left(m_{J'}^2 - \frac{J'(J'+1)}{3} \right), \quad (1)$$

where ν_Q is a characteristic frequency proportional to the electric field gradient and the electric quadrupole moment [72], and where θ is the angle between the electric field gradient principal axis and the quantization axis defined by the applied magnetic field. J' refers to the upper $^2D_{5/2}$ state of the transition; the lower $^2S_{1/2}$ state has no quadrupole moment. Δf_Q also describes the line-center shift of symmetric pairs since the two components of any pair have the same $|m_{J'}|$, as seen earlier.

In Eq. (1) we have omitted the effect of asymmetry in the trap potential [13,71]. This asymmetry is responsible for the small difference observed between the radial secular frequencies ω_X and ω_Y . Its relative contribution to Δf_Q is less than 1% in our system, and it has no effect on the electric quadrupole shift cancellation methods described later in this section.

We have investigated the electric quadrupole shift in the new end-cap trap. Data taken at four directions of the magnetic field are shown in Fig. 5. This graph illustrates clearly the linear dependence of Δf_Q on $m_{J'}^2$, and the variation of slope with the quantization axis direction.

Note that an $m_{J'}^2$ dependence arises also from the tensor Stark shift caused by micromotion as discussed in Sec. IV B3. With minimization of micromotion, the tensor Stark shift on the Zeeman pair with the greatest shift sensitivity is reduced to a level of $<4 \times 10^{-17}$ in the present work. The tensor Stark shift contribution in Fig. 5 is therefore two to three orders of magnitude smaller than that of the electric quadrupole shift and can be safely ignored in the analysis. It must be observed that these shifts on Zeeman components with a specific value of $m_{J'}^2$, caused by either the electric quadrupole effect or the tensor Stark effect, are not representative of the final uncertainties. The cancellation method presented later in this section reduces these shifts by several orders of magnitude.

The electric field gradient direction and ν_Q were determined from the data shown in Fig. 5 and from a few more data sets not shown here. Fitting Eq. (1) to the data, we find that the field gradient is aligned approximately along the axis of the end-cap electrodes and that $\nu_Q = -5.0(3)$ Hz. From Eq. (1), we find that the largest shift occurs for $\theta = 0^\circ$ and $|m_{J'}| = 5/2$. For our trap, $|\Delta f_Q|_{\max} = 8.3$ Hz. This maximum shift condition is nearly obtained with the field B2 in Fig. 5.

These important shifts caused by patch potentials on the end-cap electrodes can fortunately be canceled to an

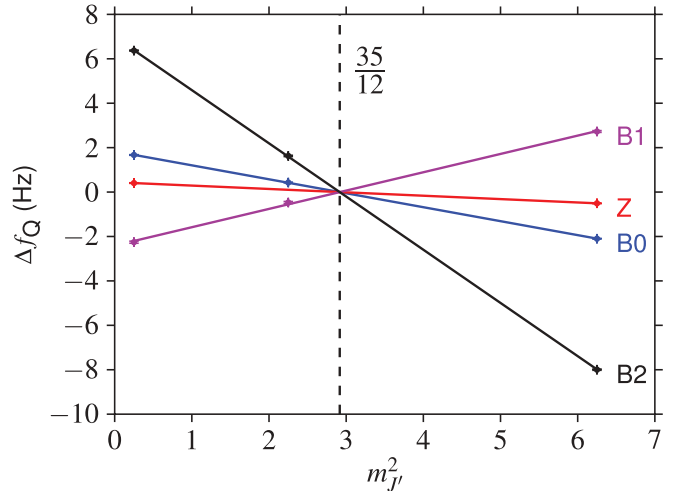


FIG. 5. (Color online) Electric quadrupole shift, Δf_Q , as a function of $m_{J'}^2$. The four data sets shown were measured with different quantization axis directions. The first, second, and fourth Zeeman pairs, with $|m_{J'}| = 1/2, 3/2,$ and $5/2$, were selected for the measurements at magnetic field directions labeled B0, B1, and B2. For the Z direction, only first and fourth pairs were measured. The field in our experiments is usually B0. For $^{88}\text{Sr}^+$ the electric quadrupole shift is canceled at the intercept of $m_{J'}^2 = 35/12$. Note that only the relative frequency shifts are reported in this figure; the intercepts at $m_{J'}^2 = 35/12$ all occur intentionally at $\Delta f_Q = 0$.

extremely high level. Several methods have been proposed to cancel this shift. A first method uses the average of the line center of one pair of components (a single component if a magnetic insensitive transition exists) for three mutually orthogonal directions of the magnetic field [71]. Another method proposes to use designed entangled states to cancel the electric quadrupole shift by averaging over states with different magnetic quantum numbers [73]. Finally, a method that we proposed cancels the electric quadrupole shift by measuring the frequencies of several pairs of components, which also has the effect of averaging over the energies of the magnetic sublevels [13].

The method that uses mutually orthogonal magnetic fields requires accurate knowledge of the magnetic field directions and magnitude for a high level of cancellation. The electric quadrupole shift of the $^{199}\text{Hg}^+$ ion standard has been reduced to a level of 10^{-17} with this method [25]. The designed entangled states cancellation method is not suitable for single-ion optical frequency standards.

All our frequency measurements are made with the method that averages the frequencies of several pairs of Zeeman components. We recall here the main aspects of the method which can be implemented two different ways. More details can be found in previous work [13,59].

The net electric quadrupole shift, Δf_Q , vanishes when averaged over the $^2D_{5/2}$ sublevels. This can be seen by summing the term in square brackets in Eq. (1) over all the excited state sublevels:

$$\sum_{m_{J'}=-J'}^{J'} \left(m_{J'}^2 - \frac{J'(J'+1)}{3} \right) = 0. \quad (2)$$

Although this conclusion was derived using an equation obtained by first-order perturbation theory, the average method actually gives an exact cancellation to all orders in perturbation theory because the Hamiltonian of the electric quadrupole shift is traceless [14,70]. The zero-trace property of the quadrupole interaction implies that the sum over the eigenvalues of the $^2D_{5/2}$ state affected by the electric quadrupole shift must be zero. This sum is realized experimentally by taking the average frequency of three pairs of Zeeman components that connect to all of the $^2D_{5/2}$ state sublevels.

An alternative method is obtained by observing that $\Delta f_Q = 0$ in Eq. (1) when $m_{J'}^2 = J'(J' + 1)/3$. For the $^2D_{5/2}$ state, $J' = 5/2$ and a null term occurs when $m_{J'}^2 = 35/12$. This suggests a method where the quadrupole-shift-free ion frequency is calculated by interpolation at the intercept $m_{J'}^2 = 35/12$. This requires the measurement of only two pairs of components instead of three. Figure 5 shows the position of the $m_{J'}^2 = 35/12$ intercept where the quadrupole shift vanishes.

The interpolation approach is, in principle, only valid to first order in perturbation theory. Nevertheless, the average of two Zeeman components in a symmetric pair cancels the second-order quadrupole shift term because it is an odd function of $m_{J'}$ [70]. This is analogous to the cancellation of the linear Zeeman effect where the shifts are also odd functions of the magnetic quantum number. The interpolation method starts to fail at the third-order term only. For a magnetic field of $2 \mu\text{T}$, the third-order term causes deviations from the linear dependence on $m_{J'}^2$, at an estimated level of $\lesssim 10^{-8}$ Hz. From a practical viewpoint, whether the interpolation or the exact averaging method is used, the accuracy of the results will not be affected.

In our experiments, the quadrupole shift cancellation is implemented by averaging three pairs of Zeeman components, specifically the first, second, and fourth pairs (see Fig. 2). This was the case for the fields B0, B1, and B2 in Fig. 5, where data points at all the possible $m_{J'}^2$ are present. The measurement at the field labeled Z was performed using the interpolation approach. An advantage of interpolation over averaging is a shorter cycling time through the components. On the other hand, measurement of three pairs of components provides a diagnostic of the lock performance as the three center frequencies must follow a linear dependence on $m_{J'}^2$.

The algorithm for the lock to the ion continually cycles through the two or three pairs of components. Consequently, the quadrupole shift is being continuously evaluated during a frequency measurement with the expected result of an extremely small uncertainty in the shift cancellation. Figure 6 shows an example of the time evolution of the quadrupole shift magnitude $A_Q = \nu_Q (3 \cos^2\theta - 1)/4$ for a lock run that lasted 36 h. The average drift rate of A_Q is $\approx -1.5 \mu\text{Hz/s}$. The slow fluctuations observed over times of several hours are attributed to variations in the magnetic field and electric field gradient. For example, the peak at 15 h is correlated with a fluctuation in the magnetic field observed in the Zeeman splittings data. The short-term fluctuations are caused by measurement noise due to the limited statistics associated with probing a single ion [74], and also possibly by the servo response.

We estimate the uncertainty on the canceled electric quadrupole shift as follows. From Eq. (1) and experimental measurements of $A_Q(t)$, the effect of the quadrupole shift

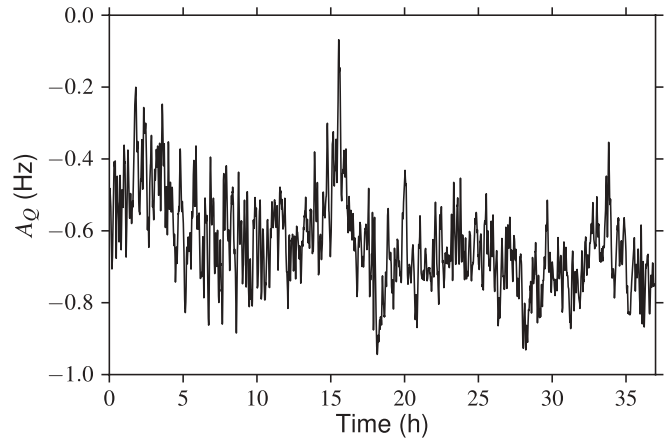


FIG. 6. Electric quadrupole shift magnitude, $A_Q = \nu_Q (3 \cos^2\theta - 1)/4$, as a function of time for the longest measurement run reported in this work. A_Q is determined experimentally using the frequency difference between shifted pairs: $A_Q = [\Delta f_Q(m_{J'} = 5/2) - \Delta f_Q(m_{J'} = 1/2)]/6$.

variations on the frequency of each Zeeman component used in the lock can be determined. These data are then used in a numerical simulation of the servo algorithm to determine the frequency error. For the data shown in Fig. 6, the simulation indicates that the cancellation method reduces the electric quadrupole shift to a fractional level of 3×10^{-19} . This is a conservative estimate given that the short-term fluctuations caused by measurement noise in the A_Q data degrade the cancellation level in the simulation.

The electric quadrupole shift on the components with the greatest shift sensitivity ($|m_{J'}| = 5/2$) is over four orders of magnitude larger than the canceled frequency uncertainty. This extremely high cancellation level will increase further with improvements of the lock to the ion line center. The quadrupole shift is therefore not expected to become an issue for the accuracy of single-ion optical frequency standards that use the cancellation method based on the continuous averaging of several pairs of Zeeman components.

B. Micromotion shifts

Micromotion is the ion movement driven by the ac electric fields of the trap. If not properly minimized, micromotion can create shifts orders of magnitude larger than all the other frequency shifts combined [13]. It is therefore paramount for an ion trap designed for operation as an optical frequency standard to allow for precise control and evaluation of the micromotion levels.

Ideally, the ion should be made to rest at the center of the trap where the electric fields and micromotion vanish. In a real trap, however, several effects can cause micromotion: displacement of the ion from the trap center by charge buildup on the trap structure and patch potentials, a phase difference between the ac voltages applied to the end-cap electrodes, and the secular motion of the ion driven by its thermal energy [75]. Minimization is performed in a different manner in each case; the displacement is minimized with voltages applied to trim electrodes, the phase difference is minimized with a phase

shifter, and the secular motion is reduced by lowering the ion temperature.

Regardless of the cause, micromotion produces Stark shifts and second-order Doppler shifts. These two types of shifts are strongly correlated as they are produced by the same electric force acting on the ion.

1. Measurement of micromotion

The ion micromotion modulates the frequency of the Zeeman components by the first-order Doppler effect, thus creating sidebands on the Zeeman spectrum at the trap frequency Ω . The amount of micromotion along the laser-beam direction can be determined from the sideband-to-carrier intensity ratio of a Zeeman component. For a small modulation index β_i , the ratio is [75]

$$R_i = \frac{J_1^2(\beta_i)}{J_0^2(\beta_i)} \cong \frac{\beta_i^2}{4}, \quad (3)$$

where $J_0^2(\beta_i)$ and $J_1^2(\beta_i)$ are, respectively, the normalized intensities of the carrier and first sidebands of the Zeeman component under study and J_n are Bessel functions of order n . The laser-beam direction i can be any of the three mutually orthogonal directions of the probe laser beam. The relation between \mathbf{v}_0 , the vector amplitude of the ion velocity at the angular frequency Ω , and the modulation index is given by

$$\beta_i = \left(\frac{\omega_0}{\Omega} \right) \frac{|\hat{\mathbf{n}}_i \cdot \mathbf{v}_0|}{c}, \quad (4)$$

where ω_0 is the probe laser angular frequency, $\hat{\mathbf{n}}_i$ a unit vector in the direction of propagation of the laser beam, and c the speed of light. A simple application of the equations of motion give $\mathbf{E}_0 = (m\Omega/e)\mathbf{v}_0$, where \mathbf{E}_0 is the vector amplitude of the electric field. m and e are, respectively, the mass and charge of the ion. This relation provides a connection between modulation index and electric field.

The quantity of interest for the micromotion shifts is the mean-squared value of the electric field, $\langle E^2(t) \rangle = E_0^2/2$. From a measurement along a single direction, it is not possible to determine $\langle E^2(t) \rangle$ as the angle between the laser beam and the ion motion is unknown. Summing over measurements made along three orthogonal directions provides a simple relationship between the sideband-to-carrier intensity measurements and the electric field:

$$\langle E^2(t) \rangle = 2 \left(\frac{m\Omega^2 c}{e\omega_0} \right)^2 \sum_{x,y,z} R_i. \quad (5)$$

Minimizing micromotion simply amounts to minimizing the sum of the micromotion sideband intensity ratios, $\sum R_i$.

2. Minimization of micromotion

Initially, the largest contribution to micromotion in the new end-cap trap was the phase difference φ_{ac} between the end-cap electrodes. The phase was adjusted by trimming the lengths of the external conductors connected to the end-cap electrodes until a minimum in the micromotion was found.

With φ_{ac} permanently minimized, the only adjustment required is positioning of the ion at the trap center with the trim electrode voltages. The micromotion is minimized in two

steps to save time. First, a coarse adjustment is performed by monitoring the ion motion with the camera while the trap depth is alternated at a rate of 0.5 Hz between strong and weak confinements. The displacement of the ion caused by confinement modulation is then minimized by varying the trim electrode voltages until no discernible motion is observed [14]. This method has good sensitivity in the plane seen by the camera, but poor sensitivity along the viewing axis. Nevertheless, the method removes most of the ion micromotion in a very short time.

In the second step, the micromotion is measured with the sideband-to-carrier intensity ratios method described in the previous section. If the micromotion levels are not optimum, the trim voltages are adjusted and the measurement repeated until a satisfactory solution is found. Using results from several minimization runs made on different days, we obtain $\sum R_i = 0.021(7)$. For this level of micromotion, the error made by the approximation of Eq. (3) is less than 1%, much lower than the uncertainty of the measurement.

3. Quadratic Stark shift

The frequency shift of a magnetic sublevel m_J caused by the Stark effect is given by the following relation [53,71]:

$$\Delta\nu_{\text{Stark}} = -\frac{\langle E^2 \rangle}{2h} \left(\alpha_0 + \frac{1}{2}\alpha_2(3\cos^2\phi - 1) \times \frac{[3m_J^2 - J(J+1)]}{J(2J-1)} \right), \quad (6)$$

where h is Planck's constant, and where α_0 and α_2 are, respectively, the scalar and tensor polarizabilities of the level considered. ϕ is the angle between the electric field direction and the quantization axis defined by the magnetic field. The shift observed by spectroscopy is the difference between the two levels of the transition. The scalar part of the Stark shift is thus given by

$$\Delta\nu_{\text{scalar}} = -\frac{\Delta\alpha_0}{2h} \langle E^2 \rangle, \quad (7)$$

where $\Delta\alpha_0 = \alpha_0(D_{5/2}) - \alpha_0(S_{1/2})$.

The frequency shift caused by the tensor part of the Stark effect has a contribution only from the $^2D_{5/2}$ state; the tensor polarizability of the $^2S_{1/2}$ state is zero. Using $J' = 5/2$ in Eq. (6), the shift of a Zeeman component with upper state magnetic quantum number $m_{J'}$ is

$$\Delta\nu_{\text{tensor}}(m_{J'}) = -\left(\frac{3}{40h} \right) \alpha_2(D_{5/2}) (3\cos^2\phi - 1) \times \left(m_{J'}^2 - \frac{35}{12} \right) \langle E^2 \rangle. \quad (8)$$

When considering the shift on the S - D transition line center, we must take into account the averaging method used to cancel the electric quadrupole shift. The averaging has no effect on $\Delta\nu_{\text{scalar}}$ as all the sublevels are shifted by the same amount. The tensor shift, however, has exactly the same dependence on $m_{J'}$, as that of the electric quadrupole shift as seen by comparing Eqs. (1) and (8). Consequently, $\Delta\nu_{\text{tensor}}$ is canceled by an estimated four orders of magnitude by this method, regardless of the micromotion level.

Combining Eqs. (5) and (7), we obtain for the fractional scalar Stark shift of the S - D transition:

$$\frac{\Delta v_{\text{scalar}}}{\nu_0} = -\frac{\Delta\alpha_0}{\hbar\omega_0} \left(\frac{m\Omega^2 c}{e\omega_0} \right)^2 \sum_{x,y,z} R_i, \quad (9)$$

where $\nu_0 = \omega_0/2\pi$ is the clock transition frequency in Hz, $\hbar = h/2\pi$, and $\Delta\alpha_0 = -4.83(17) \times 10^{-40}$ J m²/V² for the ⁸⁸Sr⁺ ion [55]. Our trap was operated at a frequency of $\Omega = 2\pi \times 14.39$ MHz. Replacing these values and the other physical constants in Eq. (9), the fractional frequency shift caused by the scalar Stark effect is $1.05(4) \times 10^{-15} \sum R_i$. For the typical level of minimization that we achieve, $\Delta v_{\text{scalar}}/\nu_0 = 2.2(7) \times 10^{-17}$. The discussion of the net micromotion shift and uncertainty is postponed to Sec. IV B 5 because of the correlation between the scalar Stark and second-order Doppler shifts.

To obtain an estimate of the uncertainty on the tensor Stark shift, we evaluate the maximum possible shift and apply the suppression factor of $\approx 10^4$ estimated for the electric quadrupole shift in Sec. IV A. The maximum occurs for the symmetric Zeeman pair with $|m_{J'}| = 5/2$ and for $\phi = 0^\circ$. Replacing these values in Eq. (8) and using Eq. (5), we obtain

$$\left(\frac{\Delta v_{\text{tensor}}}{\nu_0} \right)_{\text{max}} = -\frac{\alpha_2}{\hbar\omega_0} \left(\frac{m\Omega^2 c}{e\omega_0} \right)^2 \sum_{x,y,z} R_i. \quad (10)$$

Using the same experimental parameters as for the scalar term, and $\alpha_2(D_{5/2}) = -7.85(5) \times 10^{-40}$ J m²/V² [55], we have the relation $(\Delta v_{\text{tensor}}/\nu_0)_{\text{max}} = 1.70(1) \times 10^{-15} \sum R_i$. With $\sum R_i = 0.021(7)$, the maximum fractional shift is $4(1) \times 10^{-17}$. The quadrupole shift cancellation method reduces this value to $\approx 4 \times 10^{-21}$.

4. Second-order Doppler shift

As predicted by the special theory of relativity, the motion of the ion produces a relativistic Doppler shift that decreases the frequency observed in the laboratory [76]. The dominant shift in the Taylor expansion of the relativistic Doppler effect is the so-called second-order Doppler shift:

$$\frac{\Delta v_{\text{D2}}}{\nu_0} = -\frac{1}{2} \frac{\langle v^2 \rangle}{c^2}, \quad (11)$$

where $\langle v^2 \rangle$ is the mean-squared velocity of the ion. Equations (3) and (4) provide a direct connection to the second-order Doppler shift. Noting that we can write $|\hat{\mathbf{n}}_i \cdot \mathbf{v}_0|^2 = |\mathbf{v}_0|^2 \cos^2\theta_i = 2\cos^2\theta_i \langle v^2 \rangle$, we obtain for the sideband-to-carrier intensity ratio

$$R_i = \left(\frac{\omega_0}{\Omega} \right)^2 \frac{\langle v^2 \rangle}{2c^2} \cos^2\theta_i, \quad (12)$$

where θ_i is the angle between $\hat{\mathbf{n}}_i$ and \mathbf{v}_0 . Since $\sum \cos^2\theta_i = 1$, the second-order Doppler shift as a function of sideband intensity is given by

$$\frac{\Delta v_{\text{D2}}}{\nu_0} = -\left(\frac{\Omega}{\omega_0} \right)^2 \sum_{x,y,z} R_i. \quad (13)$$

For the experimental parameters provided earlier and with minimization of micromotion, the second-order Doppler shift is $\Delta v_{\text{D2}}/\nu_0 = -2.2(7) \times 10^{-17}$.

5. Scalar Stark and second-order Doppler shifts combined

The Stark and second-order Doppler shifts associated with micromotion are driven by the same electric field. As a result, they are correlated and cannot be considered separately in the uncertainty analysis. The combined micromotion shifts, $\Delta v_\mu = \Delta v_{\text{scalar}} + \Delta v_{\text{D2}}$, obtained by adding Eqs. (9) and (13) is, in fractional form,

$$\frac{\Delta v_\mu}{\nu_0} = -\left(\frac{\Omega}{\omega_0} \right)^2 \left[1 + \frac{\Delta\alpha_0}{\hbar\omega_0} \left(\frac{m\Omega c}{e} \right)^2 \right] \sum_{x,y,z} R_i. \quad (14)$$

For ions with a negative value of $\Delta\alpha_0$, such as ⁸⁸Sr⁺, the term in square brackets vanishes when the trap frequency takes the value [75]

$$\Omega_0 = \frac{e}{m c} \sqrt{\frac{\hbar\omega_0}{\Delta\alpha_0}}. \quad (15)$$

At that frequency, the scalar Stark and second-order Doppler shifts have the same magnitude but opposite signs. For ⁸⁸Sr⁺, $\Omega_0 = 2\pi \times 14.39(25)$ MHz, where the uncertainty is from $\Delta\alpha_0$. A trap frequency of 14.39 MHz was used for all the measurements reported in this work.

The level of cancellation is determined by the uncertainty on $\Delta\alpha_0$. The term in square brackets is null with an uncertainty of 0.035; the micromotion shifts are therefore suppressed by a factor of 28. When applied to micromotion shifts of $\pm 2.2(7) \times 10^{-17}$, the combined shifts are canceled down to a level of $\pm 8(3) \times 10^{-19}$. The estimated uncertainty on the total micromotion shifts is thus $\approx 1 \times 10^{-18}$.

C. Ion temperature effects

The thermal secular motion of the ion in the rf trap produces frequency shifts. Motion at the secular frequencies ω_i causes a second-order Doppler shift. During the secular motion, the ion is displaced from the trap center and experiences the rf fields of the trap, thus causing micromotion-induced second-order Doppler and Stark shifts. The treatment given below uses the pseudopotential approximation in which terms of order $(\omega_i/\Omega)^2$ are neglected. The error introduced by this assumption is about 1% for our experimental conditions.

1. Temperature measurement

The ion temperature was determined by measuring its thermal velocity using the ratios of secular sideband to carrier intensities, a method essentially identical to that used to measure micromotion.

The equations of motion in the pseudopotential take the form of a Mathieu equation. To simplify the discussion, we assume in the treatment given below that there is no micromotion caused by either ion displacement or φ_{ac} . The first-order solution to the Mathieu equation is [75,77]

$$u_i(t) = u_{0i} \cos(\omega_i t + \phi_i) \left[1 - \frac{q_i}{2} \cos(\Omega t) \right], \quad (16)$$

where $u_i(t)$ is the position of the ion along one of the principal axes of secular motion, labeled X , Y , or Z . u_{0i} is the amplitude of secular motion, ω_i its angular frequency, and ϕ_i the initial phase. In the case where there is no dc voltage applied to the end-cap electrodes, the parameters q_i are given by

$$q_X = q_Y = -\frac{q_Z}{2} = \frac{-4eV_0}{m\Omega^2 L (r_0^2 + 2z_0^2)}, \quad (17)$$

where V_0 is the amplitude of the voltage applied to the trap, r_0 the radius of the end-cap electrode, and z_0 the distance between the center of the trap and the end-cap faces. L is a voltage loss factor that characterizes the departure of the end-cap trap from an ideal Paul trap [54].

The first term on the right-hand-side of Eq. (16) is the secular motion while the second term is the micromotion. The total energy of the ion is obtained by evaluating its kinetic energy using Eq. (16). Neglecting terms of order $(\omega_i/\Omega)^2$, the total energy for motion along axis i is

$$U_i = \frac{m\langle v_i^2 \rangle}{2} = \frac{m u_{0i}^2 \omega_i^2}{2}, \quad (18)$$

where $v_i = \partial u_i / \partial t$. Note that the pseudopotential energy is purely kinetic in the rf trap. The energy U_i is equal to the thermal energy of a harmonic oscillator at temperature T_i , so we have the relation

$$\frac{m u_{0i}^2 \omega_i^2}{2} \cong k T_i, \quad (19)$$

where k is Boltzmann's constant. The error introduced by using the classical rather than the quantum mechanical result for the energy of a harmonic oscillator is $30 \mu\text{K}$. This is negligible in comparison to the Doppler cooling limit of $500 \mu\text{K}$ for the $^{88}\text{Sr}^+$ ion [78].

The relation between temperature and intensity ratios is given by

$$T_i = \frac{2mc^2}{k} \left(\frac{\omega_i}{\omega_0} \right)^2 \sum_{l=x,y,z} R_{l,i}, \quad (20)$$

where $R_{l,i}$ is the sideband-to-carrier intensity ratio for laser-beam propagation direction l and secular motion along the principal axis i .

The ion temperature was evaluated for the three principal axes of motion and the results were averaged. We measured $T = 1.8(7) \text{ mK}$, which is only a factor of three higher than the Doppler cooling limit.

2. Frequency shifts

The total second-order Doppler shift is obtained by combining Eqs. (11), (18), and (19), and summing over the principal axes of motion,

$$\frac{\Delta v_{\text{D2,total}}}{\nu_0} = -\frac{3kT}{mc^2}, \quad (21)$$

where $T = \frac{1}{3} \sum T_i$. $\Delta v_{\text{D2,total}}$ contains two contributions, one from secular motion and the other from micromotion. In the pseudopotential approximation, the two contributions are equal, as expected from a conservation-of-energy argument [79]. This is confirmed by computing either contribution

separately. The second-order Doppler shifts are therefore

$$\frac{\Delta v_{\text{D2},s}}{\nu_0} = \frac{\Delta v_{\text{D2},\mu}}{\nu_0} = -\frac{3kT}{2mc^2}, \quad (22)$$

where the labels s and μ refer to secular and micromotion contributions, respectively.

For a determination of the scalar Stark shift, the mean-squared trap field $\langle E^2 \rangle$ is evaluated for an ion motion described by Eq. (16). The motion amplitude is determined by temperature according to Eq. (19). Inserting the $\langle E^2 \rangle$ obtained in Eq. (7) yields

$$\frac{\Delta v_{\text{scalar},\mu}}{\nu_0} = \frac{-3kT}{2} \frac{\Delta\alpha_0}{\hbar\omega_0} \left(\frac{m\Omega^2}{e^2} \right). \quad (23)$$

$\Delta v_{\text{D2},\mu}$ and $\Delta v_{\text{scalar},\mu}$ are correlated micromotion shifts. Their sum gives the combined micromotion shift for thermal motion:

$$\frac{\Delta v_{\mu,\text{thermal}}}{\nu_0} = \frac{-3kT}{2mc^2} \left[1 + \frac{\Delta\alpha_0}{\hbar\omega_0} \left(\frac{m\Omega c}{e} \right)^2 \right]. \quad (24)$$

The term in square brackets is null at the trap frequency Ω_0 given by Eq. (15). As for micromotion from ion displacement, the uncertainty on the combined shifts is given by the magnitude of either shift taken separately, 2.8×10^{-18} for a temperature of $1.8(7) \text{ mK}$, suppressed by a factor of 28. The uncertainty on $\Delta v_{\mu,\text{thermal}}/\nu_0$ is therefore 1×10^{-19} . We do not need to consider that contribution separately from the other micromotion shifts in the uncertainty budget as it is already included in the measurements of Sec. IV B1. The only new shift that needs to be included is the second-order Doppler shift caused only by the secular movement: $\Delta v_{\text{D2},s}/\nu_0 = -3(1) \times 10^{-18}$.

D. ac Stark shifts

Electromagnetic radiation interacting with the ion causes ac Stark shifts of the clock transition. In Sec. IV D1 the shifts caused by off-resonant coupling to laser radiation during the probing period are evaluated. This includes radiation from the probe laser at 674 nm and the repumper laser at 1092 nm . The ac Stark shift caused by near-resonant dipole coupling to the cooling laser radiation at 422 nm is treated in Sec. IV D2, and the effect of blackbody radiation is discussed in Sec. IV E.

1. 674 and 1092 nm

Only the scalar part of the Stark shift caused by off-resonant dipole coupling is considered here because the tensor part is canceled as explained in Sec. IV B3. The scalar Stark shift is given by Eq. (7), with replacement of $\Delta\alpha_0$ by the appropriate differential ac scalar polarizability

$$\Delta v_{\text{ac}}(\lambda) = -\frac{\Delta\alpha_{\text{ac}}(\lambda)}{2hc\epsilon_0} I = \kappa(\lambda) I, \quad (25)$$

where $\Delta\alpha_{\text{ac}}(\lambda) = \alpha_{\text{ac}}(D_{5/2},\lambda) - \alpha_{\text{ac}}(S_{1/2},\lambda)$. λ is the laser wavelength, ϵ_0 the vacuum permittivity, and $\kappa(\lambda)$ a convenient intensity shift coefficient. We used the relation $I = c\epsilon_0\langle E^2 \rangle$ to convert from mean-squared field to light intensity.

The intensity shift coefficients were estimated in [53]: $\kappa(674 \text{ nm}) = 0.8(2) \text{ mHz}/(\text{W}/\text{m}^2)$ and $\kappa(1092 \text{ nm}) = -1.6(4) \text{ mHz}/(\text{W}/\text{m}^2)$. Using the intensities reported in

Table I for the probing period, the ac Stark shifts at 674 and 1092 nm are, respectively, 16(9) μHz and $-2(1)$ mHz, or, in fractional terms, $4(2) \times 10^{-20}$ and $-4(2) \times 10^{-18}$.

Laser light at 674 nm also causes ac Stark shifts by quadrupole coupling with off-resonant Zeeman components of the S - D manifold [80–83]. These shifts, which are on the order of ± 300 μHz for our experimental conditions, change the splittings of symmetric pairs, but not their center frequencies.

2. 422 nm

The S - P cooling transition shares a common ground state with the S - D clock transition. As a consequence, residual light from the cooling laser at 422 nm, which is nearly resonant with the S - P transition, can potentially create a large scalar ac Stark shift on the clock transition. The tensor Stark shift is several orders of magnitude lower because the D state only interacts with 422-nm radiation by off-resonant coupling. In addition, it is canceled by the measurement method used to eliminate the electric quadrupole shift.

In the low intensity limit ($|\Omega_{ge}| \ll \Gamma$), the ac Stark shift of the ground state as a function of detuning is given by [84,85]

$$\Delta\omega_g = \left(\frac{\Omega_{ge}}{\Gamma}\right)^2 \frac{\delta}{1 + (2\delta/\Gamma)^2}, \quad (26)$$

where Ω_{ge} is the Rabi frequency for a transition between a magnetic sublevel of the ground state and a magnetic sublevel of the excited state. Γ is the excited-state population decay rate and δ the detuning given by the difference between the laser frequency and the transition frequency. The frequency units are in rad/s in the above equation.

The Rabi frequency is defined as $\Omega_{ge} = \mu_{ge} E_0/\hbar$, where μ_{ge} is the dipole moment between the magnetic sublevels of the transition and E_0 the amplitude of the laser light electric field. μ_{ge} is conveniently calculated using the reduced electric dipole matrix element [52,80].

For the specific case of the $^2S_{1/2}$ - $^2P_{1/2}$ cooling transition of $^{88}\text{Sr}^+$, $\Gamma = 135.58 \times 10^6/\text{s}$ and the reduced dipole matrix element is $3.078 ea_0$, where a_0 is the Bohr radius [55]. The detuning in our experiments was $\delta = -\Gamma/2$. Using the relation $I = c \epsilon_0 E_0^2/2$ between intensity and electric field amplitude, we obtain $(\Omega_{ge}/\Gamma)^2 = 4.18 \times 10^{-4} I$ for $\Delta m = 0$ transitions and $8.37 \times 10^{-4} I$ for $\Delta m = \pm 1$ transitions. I is in W/m^2 . The intensity shift coefficients for the clock transition frequency, given by $-\Delta\omega_g/(2\pi I)$, are 2.26 $\text{kHz}/(\text{W}/\text{m}^2)$ for $\Delta m = 0$ transitions, and 4.51 $\text{kHz}/(\text{W}/\text{m}^2)$ for $\Delta m = \pm 1$ transitions. For comparison, the intensity shift coefficients for 674- and 1092-nm radiation are six orders of magnitude smaller.

Using the 422-nm scattered light intensity of $7(7) \times 10^{-10}$ W/m^2 reported in Table I and the largest intensity shift coefficient, the clock frequency is increased by at most $3(3)$ μHz , or $7(7) \times 10^{-21}$ in fractional frequency units.

E. Blackbody radiation shift

The average electric field radiated by a blackbody at thermal equilibrium is [86]

$$\langle E^2 \rangle = (831.9 \text{ V/m})^2 \left(\frac{T}{300}\right)^4, \quad (27)$$

where T is the temperature in K. As before, $\langle E^2 \rangle$ produces a Stark shift according to Eq. (7), but with $\Delta\alpha_0$ modified to take into account the effect of the frequency distribution of the blackbody field:

$$\Delta\alpha'_0 = (1 + \eta) \Delta\alpha_0. \quad (28)$$

η is an effective dynamic correction coefficient estimated at -0.01 for the S - D transition of $^{88}\text{Sr}^+$ [55].

When the trap is in operation, the electrodes are heated by the applied rf currents. As a result, the contribution to the electric field from each surface must be evaluated. If we ignore reflections for the moment, the mean-squared field at the ion produced by a surface A is

$$\langle E_A^2 \rangle = \epsilon_A \frac{\Omega_A}{4\pi} (831.9)^2 \left(\frac{T_A}{300}\right)^4, \quad (29)$$

where ϵ_A is total normal emissivity, Ω_A the solid angle seen by the ion, and T_A the surface temperature in K. The angular dependence of ϵ_A is neglected in this equation, an assumption verified to be valid at the 0.1% level for our trap geometry and materials.

For each element of solid angle $d\Omega_A$ seen by the ion, the direct contributions from unobstructed surfaces and the contributions from other surfaces reflected into this solid angle are taken into account. To obtain the total radiation at the ion, contributions with up to 1000 multiple reflections on the electrodes are included in the calculation. The highest number of reflections is obtained when the direction of propagation of the blackbody radiation is near normal incidence on the polished and parallel end-cap electrode surfaces. All the contributions are added to provide the total mean-squared electric field at the ion for a determination of the blackbody shift of the clock transition.

The temperatures of the trap components as a function of applied voltage were investigated experimentally by using a second trap in vacuum, almost identical to the one used for the optical frequency standard. The temperatures of the end-cap electrodes, alumina spacer, and shield electrodes (see Fig. 4) were measured with a small thermistor (1 mm diameter) in three series of experiments. Each time, the thermistor was positioned at the center of the trap and the components of interest brought into contact with the thermistor by sliding them ≈ 0.5 mm beyond the other components. The temperatures measured at the nominal trap voltage of 212 V amplitude are summarized in Table II. We assigned an uncertainty of 10 $^\circ\text{C}$ to these temperatures to account for possible heat exchange biases caused by the thermistor and by the differences between the support structures of the test and frequency standard traps.

The temperature of the vacuum chamber was monitored during the experiments with four calibrated thermistors. The temperature and uncertainty reported in Table II are the average and standard deviation of measurements recorded during a 2-month period.

Table II also summarizes the emissivities used in the calculations. For molybdenum (end cap) and tantalum (shield) the values from Ref. [87] were used, while for alumina the total emissivity was estimated from Ref. [88]. The emissivity of the vacuum chamber inner walls has little importance because

TABLE II. Parameters used in the blackbody radiation field model and their contributions to the frequency uncertainty.

Parameter	Value	Frequency uncertainty	
		(mHz)	(Fractional)
T walls (°C)	23.0(4)	1.1	2.53×10^{-18}
T end cap (°C)	56(10)	0.90	2.03×10^{-18}
T alumina (°C)	50(10)	4.24	9.53×10^{-18}
T shield (°C)	45(10)	0.17	0.39×10^{-18}
ϵ walls	1.0		
ϵ end cap	0.06(3)	0.78	1.76×10^{-18}
ϵ alumina	0.8(2)	2.14	4.80×10^{-18}
ϵ shield	0.06(3)	0.16	0.36×10^{-18}
$\Delta\alpha'_0$ (10^{-40} J m ² /V ²)	-4.78(17)	8.45	1.9×10^{-17}
Total		9.83	2.2×10^{-17}

a closed vessel at thermal equilibrium behaves like an ideal blackbody radiator. Deviations from this behavior could arise if a substantial fraction of the power radiated from the heated elements was reflected back to the ion by the walls. Given the low emissivity of the inner walls, estimated at ≈ 0.5 , and the very small size of the electrodes compared to that of the vacuum chamber, we can safely use unit emissivity for the vacuum chamber inner surfaces.

The uncertainties in the frequency shifts caused by each of these parameters are reported in Table II. The total fractional frequency uncertainty of 2.2×10^{-17} , obtained by adding the contributions in quadrature, is mainly from the uncertainty on $\Delta\alpha'_0$. The low sensitivity to the uncertainties in the emissivities and temperatures of the trap components is explained by the open geometry and the low emissivity of the end-cap electrodes.

The possibility that the end-cap surfaces could be coated with strontium metal from the oven was also considered. The total emissivity of strontium was estimated using a formula derived for metals that relates emissivity to resistivity and temperature [89]. Using the resistivity found in Ref. [90] at a temperature of 56 °C, the emissivity of strontium metal is estimated as 0.04, which is within the uncertainty range used for the end-cap emissivity. Consequently, no significant change in the blackbody shift is expected as a result of surface coating with strontium metal.

Table III reports the frequency shifts associated with each surface considered in the model. Using the uncertainty obtained in Table II, the total shift is 0.250(10) Hz. The temperature of a blackbody in thermal equilibrium that would cause this shift is 27(3) °C.

TABLE III. Blackbody frequency shift contributions.

Source	Frequency shift	
	(Hz)	(Fractional)
Vacuum chamber walls	0.2084	4.68×10^{-16}
Alumina spacer	0.0327	7.36×10^{-17}
End-cap electrodes	0.0074	1.67×10^{-17}
Shield electrodes	0.0013	2.92×10^{-18}
Total	0.2498	5.62×10^{-16}

F. Quadratic Zeeman shift

The quadratic Zeeman effect for the $^{88}\text{Sr}^+$ clock transition is caused by mixing of the $^2D_{5/2}$ and $^2D_{3/2}$ sublevels when the ion is exposed to a magnetic field. States with same m_J in the doublet states interact and repel each other, pushing the sublevels of the $^2D_{5/2}$ state towards higher energies [91]. The $m_J = \pm 5/2$ sublevels have no quadratic Zeeman shift because the $^2D_{3/2}$ state has no $m_J = \pm 5/2$ sublevels.

Unlike the linear first-order Zeeman shift which is canceled by the measurement method, the quadratic Zeeman effect produces a net shift in the average frequency of a symmetric pair. Its contribution must therefore be taken into account in the evaluation of the $^{88}\text{Sr}^+$ systematic shifts.

Considering the large spin-orbit energy separation of the 2D states compared to the Zeeman interaction energy, second-order perturbation theory provides very accurate results. For the $^2D_{5/2}$ state of $^{88}\text{Sr}^+$, the quadratic Zeeman shifts as a function of magnetic sublevel, $\Delta v'_{ZQ}(m_J)$, are

$$\Delta v'_{ZQ}(\pm 1/2) = \frac{6}{25} \left(\frac{[\mu_B B (g_s - 1)]^2}{h^2 \nu_{DD}} \right), \quad (30a)$$

$$\Delta v'_{ZQ}(\pm 3/2) = \frac{4}{25} \left(\frac{[\mu_B B (g_s - 1)]^2}{h^2 \nu_{DD}} \right), \quad (30b)$$

$$\Delta v'_{ZQ}(\pm 5/2) = 0. \quad (30c)$$

B is the magnetic field in T, $g_s = -g_e$ the electron spin g -factor, and μ_B the Bohr magneton in J/T. The shifts are in Hz units. The energy separation between the $^2D_{3/2}$ and the $^2D_{5/2}$ states is $\nu_{DD} = 8.404\,382$ THz.

The electric quadrupole shift cancellation method used to measure the ion frequency averages the energies of the Zeeman sublevels. The net quadratic Zeeman shift is therefore the average of Eqs. (30):

$$\Delta v_{ZQ} = \langle \Delta v'_{ZQ}(m_J) \rangle = \frac{2}{15} \left(\frac{[\mu_B B (g_s - 1)]^2}{h^2 \nu_{DD}} \right). \quad (31)$$

Equation (31) gives a frequency shift of $3.122\,25 \mu\text{Hz}/(\mu\text{T})^2$. For the background field of $2.025(3) \mu\text{T}$ used in the present experiments, the net shift is $12.80(4) \mu\text{Hz}$.

The magnetic field associated with blackbody radiation also causes a quadratic Zeeman shift. Using Eq. (27), we have for the rms fields [86]:

$$B_{\text{rms}} = \frac{E_{\text{rms}}}{c} = 2.775 \mu\text{T} \left(\frac{T}{300} \right)^2. \quad (32)$$

The blackbody field for the effective temperature of $27(3) \text{ °C}$ obtained in Sec. IV E gives $B_{\text{rms}} = 2.78(6) \mu\text{T}$ and a quadratic Zeeman shift of $24(1) \mu\text{Hz}$. The combined static and blackbody magnetic fields cause a total shift of $37(1) \mu\text{Hz}$.

G. Collisional shift

Collisions with background gas cause a frequency shift of the clock transition line center. We consider below two methods to estimate this shift [25,53]. The only common aspect of these methods is that they use the classical Langevin collision rate to describe the collision events between an ion and polarizable neutrals [92].

The partial pressures of the background gases in the vacuum chamber have been determined with a calibrated quadrupole mass analyzer: H_2 accounts for 62% of the pressure, CO for 20%, He for 10%, and other gases for the remaining 8%. For simplicity, we consider in our analysis that all the gas is composed of H_2 . The Langevin collision rate is slightly overestimated by this assumption. For a total background pressure of 16 nPa, the collision rate between neutrals and the trapped $^{88}\text{Sr}^+$ ion is $k_L \simeq 0.006/\text{s}$.

The first method relies on frequency shift measurements made on the 2D Rydberg levels of Rb as a result of collisions with Rb background gas. The frequency shift for the isoelectronic $^{88}\text{Sr}^+$ ion is estimated by modifying the result for Rb to take into account the increase in the polarization-enhanced collision rate k_L compared to the rate for neutral particles. The shift per unit pressure is estimated at $8 \times 10^4 \text{ Hz/Pa}$ [53], which gives a shift of $\Delta\nu_{\text{coll}} \simeq 0.001 \text{ Hz}$.

The second method estimates the frequency shift caused by sudden changes in the clock transition dipole phase during collisions. The maximum shift is obtained if each Langevin collision on the ion produces a $\pi/2$ phase shift. Numerical integration of the optical Bloch equations for $\pi/2$ phase shifts occurring at random times during the probe interrogation π pulses show that the mean shift is given by $0.15 k_L$ [25]. Using the rate estimated above, the shift is $\Delta\nu_{\text{coll}} \simeq 0.001 \text{ Hz}$, in agreement with the first, unrelated, method.

The second method overestimates the shift that can be expected; the actual shift is probably significantly smaller. For the uncertainty budget, the collisional shift is considered to be zero with an uncertainty given by the above estimates of 1 mHz.

H. Line-shape distortion

The line shapes of the Zeeman components can be distorted by overlapping sidebands and by the linear Zeeman effect due to changing magnetic fields.

For our experimental conditions, where the background magnetic field is $2.025 \mu\text{T}$, the outermost Zeeman components are $\pm 80 \text{ kHz}$ from line center. The first-order secular and micromotion sidebands are well outside this narrow range of frequencies and will not cause line-shape distortions.

The difference in the secular radial frequencies, however, creates weak sidebands on the Zeeman components at $\pm 20 \text{ kHz}$. Since the splitting between the inner components is 22.7 kHz , each has a sideband that is located 2 to 3 kHz away from its symmetric counterpart. The second and fourth pairs of components used during the frequency measurements do not have such sidebands in their neighborhood. Assuming an intensity of 2% for the difference sidebands relative to the carrier (the main sidebands have a 4% intensity) and a linewidth of 9 Hz for 100-ms pulses, we calculate a fractional frequency shift of $< 2 \times 10^{-19}$ for detunings of 60 Hz or more. The shift is completely negligible for detunings of kHz. Nevertheless, care should be taken to ensure that the nominal frequency separations between sidebands and the measured components are sufficiently large to avoid accidental overlaps caused by drifts in the Zeeman splittings during a measurement.

Power-line sidebands at $\pm 60 \text{ Hz}$ have a relative intensity estimated at $< 2\%$, comparable to the value used above to

analyze the effect of the radial secular sidebands. The shifts are therefore very small. When one also takes into account that there are two symmetric sidebands on each side of the carrier, then no net shift is expected.

A possible way that distortion could lead to a net shift is if a periodic magnetic field were synchronized with the measurement sequence. This is unlikely in our experimental setup as the measurement sequence is driven by an analog function generator which is not synchronized to the power-line frequency.

In all the above scenarios, any small residual shift is also greatly suppressed by the measurement method which measures symmetric pairs of Zeeman components to cancel the linear Zeeman shift. We conclude that the net effect of possible line-shape distortions on the line-center frequency can be neglected.

I. $^{88}\text{Sr}^+$ uncertainty budget

Table IV summarizes the shifts and uncertainty estimates made in the previous sections for the S - D transition frequency of $^{88}\text{Sr}^+$. The total fractional frequency uncertainty obtained by adding the contributions in quadrature is 2.3×10^{-17} .

The electric quadrupole and tensor Stark shifts were estimated for a single measurement run of about 36 h. More measurements would reduce their quoted uncertainties further; this would, however, have no impact on the final result. All the other uncertainties are independent of the duration and number of measurements made; they represent a limit in our current knowledge of the trapped ion system. Note that the 1092-nm ac Stark shift can be eliminated altogether by using a chopper with better attenuation.

The blackbody radiation shift is the largest contributor to the total uncertainty. It is not a fundamental limit for the $^{88}\text{Sr}^+$ ion system. With an accurate measurement of the scalar polarizability $\Delta\alpha'_0$, and a more accurate model of the blackbody field at the ion, the total uncertainty has the potential to reach the low 10^{-18} uncertainty level.

V. FREQUENCY MEASUREMENT

As reported recently, the absolute frequency of the $^{88}\text{Sr}^+$ S - D transition was measured by comparing the frequency of the probe laser to an active hydrogen maser referenced to the SI second using Circular-T reports from the BIPM [48]. The link between the optical and rf standards was realized by measuring the probe laser frequency with an erbium-doped fiber laser frequency comb (femtocomb) referenced to the maser [93].

In the following sections, the corrections and uncertainties related to the absolute frequency measurement are presented. These uncertainties were not considered as part of the ion uncertainty budget presented earlier because they affect only the frequency comparison between clocks. A brief discussion of the stability of the lock to the ion line center is also given in Sec. VE.

A. Maser frequency

The frequency offset of the maser from the SI second was measured through a continuous international GPS satellite

TABLE IV. Shifts and uncertainties of the $^{88}\text{Sr}^+$ ion S - D frequency.

Source	Frequency shift		Frequency uncertainty	
	(mHz)	(Fractional)	(mHz)	(Fractional)
Blackbody radiation shift	250	5.62×10^{-16}	10	2.2×10^{-17}
Total micromotion shifts	0.0	0×10^{-18}	0.5	1×10^{-18}
ac Stark shifts				
1092 nm	-2	-4×10^{-18}	1	2×10^{-18}
674 nm	0.016	4×10^{-20}	0.009	2×10^{-20}
422 nm	0.003	7×10^{-21}	0.003	7×10^{-21}
Second-order Doppler (thermal)	-1.3	-3×10^{-18}	0.5	1×10^{-18}
Electric quadrupole shift	0.0	0×10^{-19}	0.14	3×10^{-19}
Tensor Stark shift	0.0	0×10^{-21}	0.002	4×10^{-21}
Quadratic Zeeman shifts				
Blackbody radiation	0.024	5.4×10^{-20}	0.001	2×10^{-21}
Applied field ^a	0.012 80	2.9×10^{-20}	0.000 04	9×10^{-23}
Collisional shift	0.0	0×10^{-18}	1	2×10^{-18}
Total shifts	247	5.54×10^{-16}	10	2.3×10^{-17}

^a2.025(3) μT .

intercomparison using the Department of Natural Resources Canada Precise Point Positioning data processing technique [94]. With this method, the maser frequency can be referenced to the SI second with a fractional uncertainty of 2×10^{-15} . To obtain the ion frequency at the reference potential defined by the geoid, we apply a gravitational time dilation correction, as discussed in the next section.

B. Gravitational time dilation

In our measurements, the maser frequency was referenced to the SI second so it was necessary to account for the differential gravitational time dilation experienced by the ion. The time dilation was determined from the local gravitational acceleration measured using a calibrated gravimeter [95] and the height of the ion above the geoid determined with surveying measurements relative to a GPS antenna mounted on the roof of the building [96]. The surface taken as reference for the geoid is the Canadian Gravimetric Geoid Model 2005 (CGG2005) [97].

The gravitational potential changes the ion frequency according to

$$\frac{\Delta\nu_G}{\nu_0} = \frac{gH}{c^2}, \quad (33)$$

where $g = 9.8062 \text{ m/s}^2$ is the local gravitational acceleration, and $H = 95.36(5) \text{ m}$ is the height of the frequency standard above the geoid. The frequency of the $^{88}\text{Sr}^+$ ion clock transition in the laboratory is therefore higher by $\Delta\nu_G = 4.628(2) \text{ Hz}$ compared to its value on the reference potential. In fractional frequency units, the uncertainty introduced by the evaluation of the gravitational time dilation is 5×10^{-18} .

C. Servo tracking error

The probe laser is locked to the $^{88}\text{Sr}^+$ ion line center by measuring, in rotation, the frequencies of the Zeeman components that belong to the symmetric pairs selected for the electric quadrupole shift cancellation method. More

specifically, the frequency of a single component is measured by first predicting its current line center based on the previous value, the elapsed time since that measurement was made, and the cavity drift rate. With a double-pass AOM controlled by a computer, the laser is then detuned from the predicted line center by $\pm\delta \text{ Hz}$, where δ is approximately half a linewidth, for measurement of the quantum jump rates. The imbalance in the rates provides an error signal, which, after multiplication by a suitable gain factor G , yields a new frequency estimate for the component [47].

In principle, one can choose δ and G such that the correction is exact for a given resonance line shape. An error in the drift-rate compensation, however, causes an offset between the predicted and actual line centers and a deterioration in the correction accuracy due to a change in gain with detuning. This was an issue for the measurements reported here because the servo algorithm used a constant value to compensate for a variable cavity drift rate. Figure 7 shows an example where deviations of up to 3.7 mHz/s were observed. For a cycle time of 200 s, typical for our current setup, the predicted line center was detuned by up to 0.7 Hz from the true line center.

Each measurement run reported in the next section was simulated numerically to estimate its overall servo tracking error. The simulation took into account the servo parameters used, the resonance line shape, and the drift rates derived from the frequency measurement data. After the corrections were applied to all the data, the measured ion frequency decreased by 0.12(3) Hz. The uncertainty in the correction is caused by an uncertainty in the resonance linewidths estimated at $\pm 5\%$; the other servo parameters are either exact or known with much greater accuracy.

The fractional uncertainty of 7×10^{-17} contributed by the servo errors is small in the context of the frequency measurement, but quite significant compared to the clock transition uncertainty reported in Table IV. Fortunately, the servo tracking errors can be reduced below the mHz level ($< 2 \times 10^{-18}$) with a second-order algorithm [98,99].

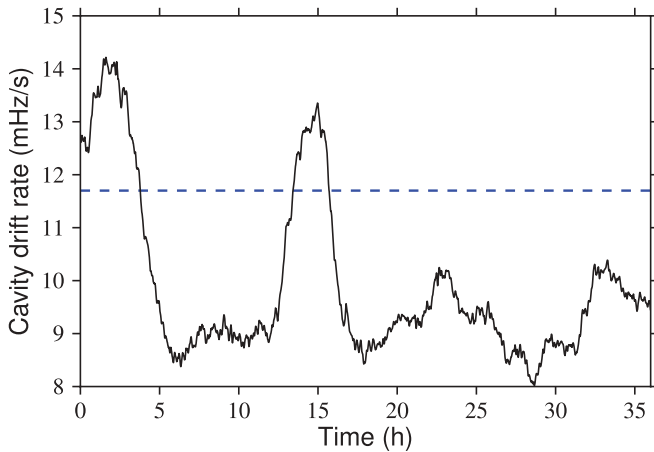


FIG. 7. (Color online) Example showing variations in the drift rate of the ultrastable ULE cavity as a function of time. The solid curve is the drift rate of the reference cavity calculated from the data of a lock run. The dashed line is the compensation drift rate used during the lock. A numerical simulation predicts an error of 60 mHz for this measurement.

D. Results

Figure 8 gives a summary of the $^{88}\text{Sr}^+$ ion clock transition frequency measurements made during a 2-month period with the new end-cap trap [48]. Each measurement is corrected for the total shift reported in Table IV, the servo tracking error, and the gravitational time dilation shift. The error bars were evaluated from the Allan deviations of the femtocomb measurements, using the ion as a reference. The stability of the lock to the ion is significantly better than that of the maser at all averaging times, as shown in Fig. 9. This approach effectively measures the stability of the maser and of the link between the maser and the femtocomb. In the example given in Fig. 9,

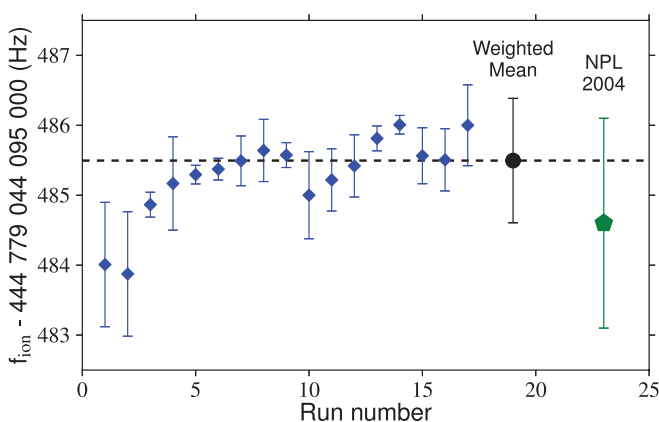


FIG. 8. (Color online) The measured $^{88}\text{Sr}^+$ ion S - D center frequencies, f_{ion} , as a function of run number are shown as diamonds. (For a display as a function of time, see [48].) The frequencies are corrected for the shifts reported in Table IV, the servo tracking errors, the gravitational time dilation shift, and the maser offset. The solid circle is the weighted mean of the data, with error bars determined by the uncertainty on the maser frequency. The pentagon is a measurement of the S - D frequency made by the NPL group with a cesium fountain [12].

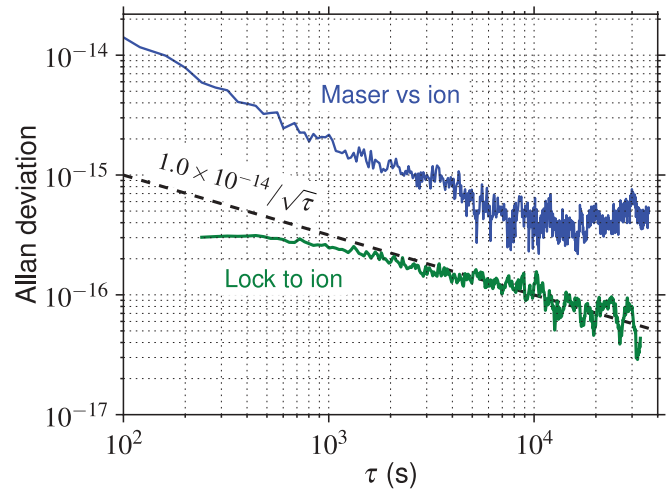


FIG. 9. (Color online) Allan deviation as a function of averaging time τ . The curve labeled “Maser vs ion” is the Allan deviation of the hydrogen maser measured using the ion as reference. The curve labeled “Lock to ion” is the estimated Allan deviation for the lock to the ion line center (see text). The lock stability of $1 \times 10^{-14}/\sqrt{\tau}$ is shown by the dashed line.

the curve labeled “Maser vs ion” shows that the statistical uncertainty for that measurement is $\approx 4 \times 10^{-16}$ or 0.2 Hz.

The statistical uncertainty in the weighted mean for the data of Fig. 8 is 0.1 Hz or 2×10^{-16} in fractional frequency units. Such a low statistical uncertainty indicates that the maser frequency variations were well accounted for. The final uncertainty is essentially given by the 0.9-Hz maser calibration accuracy. The frequency obtained with these measurements of the $^{88}\text{Sr}^+$ ion S - D transition is 444 779 044 095 485.5(9)Hz. This value is in excellent agreement with a measurement made by the NPL with a cesium fountain: 444 779 044 095 484.6(1.5)Hz [12].

E. Lock stability

The “Lock to ion” curve in Fig. 9 was obtained by calculating the Allan deviation of the frequency difference between two symmetric pairs of components for the same lock run, and by dividing by $\sqrt{6}$. This factor corrects for the noise increase caused by comparing two similar signals and for the expected stability of the line-center data which is based on three pairs of components. The obtained stability of $1 \times 10^{-14}/\sqrt{\tau}$ is in agreement with an estimate made with the reference Fabry-Perot cavity [100]. It takes 2.2 days of averaging to reach the estimated ion uncertainty of 2.3×10^{-17} . For comparison, the total measurement time of the data reported in Fig. 8 was 4.3 days. The current system is therefore already at a development stage where comparison with an equally stable optical frequency standard could be made at the uncertainty limit of the $^{88}\text{Sr}^+$ frequency standard.

There are several possible improvements that can be made to the stability of the lock to the S - D transition. For example, the quantum jump rate can be increased by a factor of ≈ 4 from the current level with state preparation and the use of a clear out laser (see Fig. 1). In addition to a better lock accuracy, optimization of the servo algorithm and parameters is also expected to result in better stability. A factor of 2 improvement

in stability from the expected increase in quantum jump rate implies that the line center of the S - D transition could be realized with a fractional frequency uncertainty of 2×10^{-17} in one day of averaging.

VI. CONCLUSIONS

We have presented a detailed analysis of the known sources of frequency shifts and their uncertainties for the $^{88}\text{Sr}^+$ single-ion optical frequency standard. The total fractional uncertainty on the shifts, estimated at 2.3×10^{-17} for the new end-cap trap, is an order of magnitude lower than previously achieved for $^{88}\text{Sr}^+$ [12] and three orders of magnitude lower than achieved with our previous system based on an rf Paul trap [13].

Several key measurement methods were implemented to minimize the uncertainties. The cancellation method based on the average of several pairs of Zeeman components essentially eliminates the electric quadrupole and tensor Stark shifts. It also simplifies the evaluation of other shifts by removing any magnetic sublevel dependence. The new system provides optical access along three mutually orthogonal axes for measurement and minimization of micromotion and measurement of secular motion. With a trap frequency chosen such that the second-order Doppler and scalar Stark shifts cancel each other, the total micromotion shifts have been reduced to the 10^{-18} level. The blackbody shift uncertainty was reduced by an order of magnitude with a recent theoretical evaluation of the scalar polarizability coefficients of the clock transition and with a model of the blackbody field at the ion based on temperature measurements on a similar trap.

The special choice of trap frequency and the quadrupole shift cancellation method make the $^{88}\text{Sr}^+$ optical frequency standard especially robust against electric field variations in the trap environment and make it a promising candidate for a practical clock and a potential primary standard. Other ion

systems can also benefit from these methods depending on the measurement strategy adopted. The reduction of micromotion shifts with trap frequency is only possible if $\Delta\alpha_0$ is negative [see Eq. (15)].

Based on our current understanding of the $^{88}\text{Sr}^+$ S - D clock transition shifts, it appears possible to obtain a fractional uncertainty in the low 10^{-18} level. For example, if the uncertainty on $\Delta\alpha'_0$ can be reduced by a factor of 10, and assuming that the blackbody field can be estimated with sufficient accuracy, the total uncertainty in Table IV reduces to 3.6×10^{-18} . For this estimate, the uncertainty on the 1092-nm light shift was set to zero as it is experimentally a simple matter to achieve this result.

The frequency of the S - D transition was recently measured against the SI second [48]. The sources of uncertainty associated with this measurement were discussed in the current work and were shown to be dominated by the rf standard fractional calibration accuracy of 2×10^{-15} . By comparison, the uncertainty on the systematic shifts of the $^{88}\text{Sr}^+$ ion clock transition is two orders of magnitude lower.

ACKNOWLEDGMENTS

The authors thank M. Gertsvolf for providing the maser frequency calibrations, L. Marmet for helpful discussions and a careful reading of the manuscript, T. Lindvall for useful discussions about ac Stark shifts, and B. Hoger and W. Pakulski for their help with the construction and maintenance of the electronic systems that run our experiments. The contributions of V. Malkov towards the evaluation of the blackbody radiation shift are acknowledged. In addition, the authors thank J. Liard, J. Silliker, and A. Belzile from the Department of Natural Resources Canada for the gravimetric and leveling measurements used in the determination of the gravitational time dilation shift.

-
- [1] H. S. Margolis, *J. Phys. B* **42**, 154017 (2009).
- [2] T. P. Heavner, S. R. Jefferts, E. A. Donley, J. H. Shirley, and T. E. Parker, *Metrologia* **42**, 411 (2005).
- [3] T. E. Parker, *Metrologia* **47**, 1 (2010).
- [4] R. Li, K. Gibble, and K. Szymaniec, *Metrologia* **48**, 283 (2011).
- [5] S. Weyers, V. Gerginov, N. Nemitz, R. Li, and K. Gibble, *Metrologia* **49**, 82 (2012).
- [6] J. Guéna, M. Abgrall, D. Rovera, P. Laurent, B. Chupin, M. Lours, G. Santarelli, P. Rosenbusch, M. E. Tobar, R. Li, K. Gibble, A. Clairon, and S. Bize, *IEEE Trans. Ultrason. Ferroelectr. Freq. Control* **59**, 391 (2012), and references therein.
- [7] J. E. Bernard, A. A. Madej, L. Marmet, B. G. Whitford, K. J. Siemsen, and S. Cundy, *Phys. Rev. Lett.* **82**, 3228 (1999).
- [8] Th. Udem, J. Reichert, R. Holzwarth, and T. W. Hänsch, *Phys. Rev. Lett.* **82**, 3568 (1999).
- [9] S. A. Diddams, D. J. Jones, J. Ye, S. T. Cundiff, J. L. Hall, J. K. Ranka, R. S. Windeler, R. Holzwarth, T. Udem, and T. W. Hänsch, *Phys. Rev. Lett.* **84**, 5102 (2000).
- [10] J. Ye, T. H. Yoon, J. L. Hall, A. A. Madej, J. E. Bernard, K. J. Siemsen, L. Marmet, J.-M. Chartier, and A. Chartier, *Phys. Rev. Lett.* **85**, 3797 (2000).
- [11] Th. Udem, S. A. Diddams, K. R. Vogel, C. W. Oates, E. A. Curtis, W. D. Lee, W. M. Itano, R. E. Drullinger, J. C. Bergquist, and L. Hollberg, *Phys. Rev. Lett.* **86**, 4996 (2001).
- [12] H. S. Margolis, G. P. Barwood, G. Huang, H. A. Klein, S. N. Lea, K. Szymaniec, and P. Gill, *Science* **306**, 1355 (2004).
- [13] P. Dubé, A. A. Madej, J. E. Bernard, L. Marmet, J.-S. Boulanger, and S. Cundy, *Phys. Rev. Lett.* **95**, 033001 (2005).
- [14] T. Schneider, E. Peik, and Chr. Tamm, *Phys. Rev. Lett.* **94**, 230801 (2005).
- [15] Y. H. Wang, R. Dumke, T. Liu, A. Stejskal, Y. N. Zhao, J. Zhang, Z. H. Lu, L. J. Wang, Th. Becker, and H. Walther, *Opt. Commun.* **273**, 526 (2007).
- [16] M. Chwalla, J. Benhelm, K. Kim, G. Kirchmair, T. Monz, M. Riebe, P. Schindler, A. S. Villar, W. Hänsel, C. F. Roos, R. Blatt, M. Abgrall, G. Santarelli, G. D. Rovera, and P. Laurent, *Phys. Rev. Lett.* **102**, 023002 (2009).
- [17] K. Hosaka, S. A. Webster, A. Stannard, B. R. Walton, H. S. Margolis, and P. Gill, *Phys. Rev. A* **79**, 033403 (2009).

- [18] Chr. Tamm, S. Weyers, B. Lipphardt, and E. Peik, *Phys. Rev. A* **80**, 043403 (2009).
- [19] Y. Huang, J. Cao, P. Liu, K. Liang, B. Ou, H. Guan, X. Huang, T. Li, and K. Gao, *Phys. Rev. A* **85**, 030503 (2012).
- [20] S. A. King, R. M. Godun, S. A. Webster, H. S. Margolis, L. A. M. Johnson, K. Szymaniec, P. E. G. Baird, and P. Gill, *New J. Phys.* **14**, 013045 (2012).
- [21] W. H. Oskay, S. A. Diddams, E. A. Donley, T. M. Fortier, T. P. Heavner, L. Hollberg, W. M. Itano, S. R. Jefferts, M. J. Delaney, K. Kim, F. Levi, T. E. Parker, and J. C. Bergquist, *Phys. Rev. Lett.* **97**, 020801 (2006).
- [22] T. Rosenband, P. O. Schmidt, D. B. Hume, W. M. Itano, T. M. Fortier, J. E. Stalnaker, K. Kim, S. A. Diddams, J. C. J. Koelemeij, J. C. Bergquist, and D. J. Wineland, *Phys. Rev. Lett.* **98**, 220801 (2007).
- [23] J. E. Stalnaker, S. A. Diddams, T. M. Fortier, K. Kim, L. Hollberg, J. C. Bergquist, W. M. Itano, M. J. Delany, L. Lorini, W. H. Oskay, T. P. Heavner, S. R. Jefferts, F. Levi, T. E. Parker, and J. Shirley, *Appl. Phys. B* **89**, 167 (2007).
- [24] N. Huntemann, M. Okhapkin, B. Lipphardt, S. Weyers, Chr. Tamm, and E. Peik, *Phys. Rev. Lett.* **108**, 090801 (2012).
- [25] T. Rosenband, D. B. Hume, P. O. Schmidt, C. W. Chou, A. Brusch, L. Lorini, W. H. Oskay, R. E. Drullinger, T. M. Fortier, J. E. Stalnaker, S. A. Diddams, W. C. Swann, N. R. Newbury, W. M. Itano, D. J. Wineland, and J. C. Bergquist, *Science* **319**, 1808 (2008).
- [26] C. W. Chou, D. B. Hume, J. C. J. Koelemeij, D. J. Wineland, and T. Rosenband, *Phys. Rev. Lett.* **104**, 070802 (2010).
- [27] H. G. Dehmelt, *IEEE Trans. Instrum. Meas.* **IM-31**, 83 (1982).
- [28] H. Katori, in *Proceedings of the 6th Symposium on Frequency Standards and Metrology*, edited by P. Gill (World Scientific, Singapore, 2002), pp. 323–330.
- [29] H. Katori, *Nat. Photon* **5**, 203 (2011), and references therein.
- [30] A. D. Ludlow, T. Zelevinsky, G. K. Campbell, S. Blatt, M. M. Boyd, M. H. G. de Miranda, M. J. Martin, J. W. Thomsen, S. M. Foreman, J. Ye, T. M. Fortier, J. E. Stalnaker, S. A. Diddams, Y. L. Coq, Z. W. Barber, N. Poli, N. D. Lemke, K. M. Beck, and C. W. Oates, *Science* **319**, 1805 (2008).
- [31] G. K. Campbell, A. D. Ludlow, S. Blatt, J. W. Thomsen, M. J. Martin, M. H. G. de Miranda, T. Zelevinsky, M. M. Boyd, J. Ye, S. A. Diddams, T. P. Heavner, T. E. Parker, and S. R. Jefferts, *Metrologia* **45**, 539 (2008).
- [32] N. D. Lemke, A. D. Ludlow, Z. W. Barber, T. M. Fortier, S. A. Diddams, Y. Jiang, S. R. Jefferts, T. P. Heavner, T. E. Parker, and C. W. Oates, *Phys. Rev. Lett.* **103**, 063001 (2009).
- [33] A. Yamaguchi, M. Fujieda, M. Kumagai, H. Hachisu, S. Nagano, Y. Li, T. Ido, T. Takano, M. Takamoto, and H. Katori, *Appl. Phys. Express* **4**, 082203 (2011).
- [34] R. Le Targat, R. Gartman, L. Lorini, B. Nagorny, M. Gurov, P. Lemonde, M. Zawada, and J. Lodewyck, in *Proceedings of the IEEE International Frequency Control Symposium* (IEEE, New York, 2012), pp. 1–4.
- [35] T. L. Nicholson, M. J. Martin, J. R. Williams, B. J. Bloom, M. Bishof, M. D. Swallows, S. L. Campbell, and J. Ye, *Phys. Rev. Lett.* **109**, 230801 (2012).
- [36] P. G. Westergaard, J. Lodewyck, L. Lorini, A. Lecallier, E. A. Burt, M. Zawada, J. Millo, and P. Lemonde, *Phys. Rev. Lett.* **106**, 210801 (2011).
- [37] J. A. Sherman, N. D. Lemke, N. Hinkley, M. Pizzocaro, R. W. Fox, A. D. Ludlow, and C. W. Oates, *Phys. Rev. Lett.* **108**, 153002 (2012).
- [38] R. J. Rafac, B. C. Young, J. A. Beall, W. M. Itano, D. J. Wineland, and J. C. Bergquist, *Phys. Rev. Lett.* **85**, 2462 (2000).
- [39] M. Notcutt, L.-S. Ma, A. D. Ludlow, S. M. Foreman, J. Ye, and J. L. Hall, *Phys. Rev. A* **73**, 031804 (2006).
- [40] A. D. Ludlow, X. Huang, M. Notcutt, T. Zanon-Willette, S. M. Foreman, M. M. Boyd, S. Blatt, and J. Ye, *Opt. Lett.* **32**, 641 (2007).
- [41] S. A. Webster, M. Oxborrow, S. Pugla, J. Millo, and P. Gill, *Phys. Rev. A* **77**, 033847 (2008).
- [42] P. Dubé, A. A. Madej, J. E. Bernard, L. Marmet, and A. D. Shiner, *Appl. Phys. B* **95**, 43 (2009).
- [43] J. Millo, D. V. Magalhães, C. Mandache, Y. Le Coq, E. M. L. English, P. G. Westergaard, J. Lodewyck, S. Bize, P. Lemonde, and G. Santarelli, *Phys. Rev. A* **79**, 053829 (2009).
- [44] Y. Y. Jiang, A. D. Ludlow, N. D. Lemke, R. W. Fox, J. A. Sherman, L.-S. Ma, and C. W. Oates, *Nat. Photon* **5**, 158 (2011).
- [45] S. Webster and P. Gill, *Opt. Lett.* **36**, 3572 (2011).
- [46] T. Kessler, C. Hagemann, C. Grebing, T. Legero, U. Sterr, F. Riehle, J. M. Martin, L. Chen, and J. Ye, *Nat. Photon* **6**, 687 (2012).
- [47] J. E. Bernard, L. Marmet, and A. A. Madej, *Opt. Commun.* **150**, 170 (1998).
- [48] A. A. Madej, P. Dubé, Z. Zhou, J. E. Bernard, and M. Gertsvolf, *Phys. Rev. Lett.* **109**, 203002 (2012).
- [49] D. J. Berkeland, *Rev. Sci. Instrum.* **73**, 2856 (2002).
- [50] D. J. Berkeland, D. A. Raymondson, and V. M. Tassin, *Phys. Rev. A* **69**, 052103 (2004).
- [51] E. Kirilov and S. Putterman, *Eur. Phys. J. D* **54**, 683 (2009).
- [52] T. Lindvall, M. Merimaa, I. Tittonen, and A. A. Madej, *Phys. Rev. A* **86**, 033403 (2012).
- [53] A. A. Madej, J. E. Bernard, P. Dubé, L. Marmet, and R. S. Windeler, *Phys. Rev. A* **70**, 012507 (2004).
- [54] C. A. Schrama, E. Peik, W. W. Smith, and H. Walther, *Opt. Commun.* **101**, 32 (1993).
- [55] D. Jiang, B. Arora, M. S. Safronova, and C. W. Clark, *J. Phys. B* **42**, 154020 (2009).
- [56] F. Riehle, *Physics* **5**, 126 (2012).
- [57] A. A. Madej and J. D. Sankey, *Opt. Lett.* **15**, 634 (1990).
- [58] V. Letchumanan, M. A. Wilson, P. Gill, and A. G. Sinclair, *Phys. Rev. A* **72**, 012509 (2005).
- [59] P. Dubé, A. A. Madej, J. E. Bernard, and A. D. Shiner, in *Proceedings of the IEEE International Frequency Control Symposium and Exposition* (IEEE, New York, 2006), pp. 409–414.
- [60] S. Gulde, D. Rotter, P. Barton, F. Schmidt-Kaler, R. Blatt, and W. Hogervorst, *Appl. Phys. B* **73**, 861 (2001).
- [61] M. Brownnutt, V. Letchumanan, G. Wilpers, R. C. Thompson, P. Gill, and A. G. Sinclair, *Appl. Phys. B* **87**, 411 (2007).
- [62] M. Vainio, J. Bernard, and L. Marmet, *Appl. Phys. B* **104**, 897 (2011).
- [63] M. Asano and K. Kubo, *J. Nucl. Sci. Technol.* **15**, 765 (1978).
- [64] D. A. Hite, Y. Colombe, A. C. Wilson, K. R. Brown, U. Warring, R. Jördens, J. D. Jost, K. S. McKay, D. P. Pappas, D. Leibfried, and D. J. Wineland, *Phys. Rev. Lett.* **109**, 103001 (2012).

- [65] L.-S. Ma, P. Jungner, J. Ye, and J. L. Hall, *Opt. Lett.* **19**, 1777 (1994).
- [66] B. C. Young, R. J. Rafac, J. A. Beall, F. C. Cruz, W. M. Itano, D. J. Wineland, and J. C. Bergquist, in *Laser Spectroscopy XIV International Conference*, edited by R. Blatt, J. Eschner, D. Leibfried, and F. Schmidt-Kaler (World Scientific, Singapore, 1999), pp. 61–70.
- [67] A. Shiner, Master of science thesis, York University, Toronto, Ontario, Canada, 2006.
- [68] A. D. Shiner, A. A. Madej, P. Dubé, and J. E. Bernard, *Appl. Phys. B* **89**, 595 (2007).
- [69] G. Humphrey, Master of science thesis, York University, Toronto, Ontario, Canada, 2009.
- [70] A. Abragam, *The Principles of Nuclear Magnetism*, International Series of Monographs on Physics (Oxford University Press, New York, 1978).
- [71] W. M. Itano, *J. Res. Natl. Inst. Stand. Technol.* **105**, 829 (2000).
- [72] G. P. Barwood, H. S. Margolis, G. Huang, P. Gill, and H. A. Klein, *Phys. Rev. Lett.* **93**, 133001 (2004).
- [73] C. F. Roos, M. Chwalla, K. Kim, M. Riebe, and R. Blatt, *Nature (London)* **443**, 316 (2006).
- [74] W. M. Itano, J. C. Bergquist, J. J. Bollinger, J. M. Gilligan, D. J. Heinzen, F. L. Moore, M. G. Raizen, and D. J. Wineland, *Phys. Rev. A* **47**, 3554 (1993).
- [75] D. J. Berkeland, J. D. Miller, J. C. Bergquist, W. M. Itano, and D. J. Wineland, *J. Appl. Phys.* **83**, 5025 (1998).
- [76] J. D. Jackson, *Classical Electrodynamics*, 3rd ed. (Wiley & Sons, New York, 1975).
- [77] D. J. Wineland, W. M. Itano, and R. S. Van Dyck, Jr., in *High-Resolution Spectroscopy of Stored Ions*, edited by D. Bates and B. Bederson, Advances in Atomic and Molecular Physics, Vol. 19 (Academic Press, San Diego, 1983), pp. 135–186.
- [78] A. A. Madej and J. E. Bernard, in *Frequency Measurement and Control: Advanced Techniques and Future Trends*, Springer Topics in Applied Physics, Vol. 79, edited by A. N. Luiten (Springer-Verlag, Berlin, 2001), pp. 153–194.
- [79] P. T. H. Fisk, *Rep. Prog. Phys.* **60**, 761 (1997).
- [80] D. F. V. James, *Appl. Phys. B* **66**, 181 (1998).
- [81] H. Häffner, S. Gulde, M. Riebe, G. Lancaster, C. Becher, J. Eschner, F. Schmidt-Kaler, and R. Blatt, *Phys. Rev. Lett.* **90**, 143602 (2003).
- [82] C. Champenois, M. Houssin, C. Lisowski, M. Knoop, G. Hagel, M. Vedel, and F. Vedel, *Phys. Lett. A* **331**, 298 (2004).
- [83] C. F. Roos, Ph.D. thesis, Institut für Experimentalphysik, Innsbruck, Austria, 2000.
- [84] J. Dalibard and C. Cohen-Tannoudji, *J. Opt. Soc. Am. B* **6**, 2023 (1989).
- [85] H. J. Metcalf and P. van der Straten, *Laser Cooling and Trapping* (Springer-Verlag, New York, 1999).
- [86] W. M. Itano, L. L. Lewis, and D. J. Wineland, *Phys. Rev. A* **25**, 1233 (1982).
- [87] American Institute of Physics, *American Institute of Physics Handbook*, 2nd ed. (McGraw-Hill, New-York, 1963), Chap. 6, p. 159.
- [88] D. Demange, M. Bejet, and B. Dufour, *QIRT Open Archives, 8th International Conference on Quantitative Infrared Thermography, QIRT 2006-087* (Padova, Italy, 2006).
- [89] P. D. Foote, *Bull. Bur. Stand. (US)* **11**, 607 (1915).
- [90] J. Katerberg, S. Niemeyer, D. Penning, and J. B. V. Zytveld, *J. Phys. F* **5**, L74 (1975).
- [91] G. K. Woodgate, *Elementary Atomic Structure*, 2nd ed. (Oxford University Press, Oxford, UK, 1992).
- [92] G. Gioumoussis and D. P. Stevenson, *J. Chem. Phys.* **29**, 294 (1958).
- [93] J. E. Bernard, P. Dubé, A. A. Madej, S. Cundy, J.-S. Boulanger, J. Jiang, and D. J. Jones, *Eur. Phys. J. D* **57**, 247 (2010).
- [94] D. Orgiazzi, P. Tavella, and F. Lahaye, in *Proceedings of the IEEE Frequency Control Symposium and Exposition* (IEEE, New York, 2005), pp. 337–345.
- [95] J. Liard and J. Silliker, *Gravity Measurements for the Strontium Ion Optical Frequency Standard at the National Research Council of Canada*, Technical Report (Geodetic Survey Division, Natural Resources Canada, 2011).
- [96] J. Silliker and A. Belzile, *Height Difference for the Strontium Ion Optical Frequency Standard at the Natural Research Council of Canada*, Technical Report (Geodetic Survey Division, Natural Resources Canada, 2011).
- [97] M. Véronneau and J. Huang, *The Canadian Gravimetric Geoid Model 2005 (CGG2005)*, Technical Report (Geodetic Survey Division, Natural Resources Canada, 2007).
- [98] D. J. Berkeland, J. D. Miller, J. C. Bergquist, W. M. Itano, and D. J. Wineland, *Phys. Rev. Lett.* **80**, 2089 (1998).
- [99] E. Peik, T. Schneider, and Chr. Tamm, *J. Phys. B* **39**, 145 (2006).
- [100] P. Dubé, A. A. Madej, J. E. Bernard, and Z. Zhou, in *Proceedings of the IEEE International Frequency Control Symposium* (IEEE, New York, 2012), pp. 255–260.